Effect of dynamical gravitomagnetic tides on measurability of tidal parameters for binary neutron stars using gravitational waves

Pawan Kumar Gupta,[1,2,*] Jan Steinhoff,[3,†] and Tanja Hinderer[4,‡]

[1]*Nikhef, Science Park, 1098 XG Amsterdam, Netherlands, European Union*
[2]*Institute for Gravitational and Subatomic Physics (GRASP), Department of Physics, Utrecht University, Princetonplein 1, 3584 CC Utrecht, Netherlands, European Union*
[3]*Max-Planck-Institute for Gravitational Physics (Albert-Einstein-Institute), Am Mühlenberg 1, 14476 Potsdam-Golm, Germany, European Union*
[4]*Institute for Theoretical Physics, Utrecht University, Princetonplein 5, 3584 CC Utrecht, Netherlands, European Union*

(Received 30 May 2023; accepted 2 November 2023; published 15 December 2023)

Gravitational waves (GWs) from binary neutron stars (NSs) have opened unique opportunities to constrain the nuclear equation of state by measuring tidal effects associated with the excitation of characteristic modes of the NSs. This includes gravitomagnetic modes induced by the Coriolis effect whose frequencies are proportional to the NS's spin frequency. The NS's spin orientation determines which subclass of gravitomagnetic modes are predominantly excited. We incorporate these effects in GW models needed for data analysis by encapsulating the adiabatic signatures from gravitomagnetic modes in slowly rotating NSs in an effective Love number which differs before and after a mode resonance and combining this with a known generic model for abrupt changes in the GWs at the mode resonance. This leads to an efficient approximate model that adds to a point-mass baseline and which we use to perform case studies of the impacts of gravitomagnetic effects for measurements with Cosmic Explorer, an envisioned next-generation GW detector. We quantify the extent to which neglecting (including) the effect of gravitomagnetic modes induces biases (significantly reduces statistical errors) in the measured tidal deformability parameters, which depend on the equation of state. Our results substantiate the importance of dynamical gravitomagnetic tidal effects for measurements with third-generation detectors.

DOI: 10.1103/PhysRevD.108.124040

I. INTRODUCTION

The gravitational wave (GW) discovery of the binary neutron star (NS) inspiral GW170817 [1] provided, for the first time, a purely gravitational channel for probing the properties of dense matter in NS interiors, whose equation of state remains poorly constrained [2,3]. While this event provided the first empirical constraints with GWs, more precise measurements of the equation of state will become possible as existing detectors (such as LIGO [4], Virgo [5], KAGRA [6]) improve in sensitivity in the coming years [7] and next-decade's envisioned third-generation facilities such as Einstein Telescope [8] and Cosmic Explorer [9] become operational. These next-generation detectors will have a much higher sensitivity and wider bandwidth, thus opening opportunities for transformative insights into dense matter under extreme gravity [10–12]. Realizing this science potential critically relies on accurate theoretical models of the GWs from binary systems including matter effects. Such models underpin the inference of source properties from the GW data, as reviewed in [13]. To date, GW measurements have only been sensitive to the dominant effects of NS matter on the signals that are characterized by an equation-of-state-dependent tidal deformability parameter. The relatively large statistical errors in these measurements dominated over systematic errors [14], with the latter, e.g., due to shortcomings in the modeling. However, similar measurements at a higher sensitivity or with future detectors will require models that are significantly more accurate and include more realistic physics to avoid biases in the interpretation and enable more stringent constraints on NS matter [15–20].

During a binary inspiral, the GW signatures of the properties of matter are due to spin and tidal effects. Tidal effects encompass various phenomena associated with the resonant or nonresonant excitation of characteristic oscillation modes of the NS, whose properties are set by the physics of the dense subatomic matter in their interiors. The modes are driven by the tidal fields of the companion, which vary in time due to the orbital motion. Relativistic

*p.gupta@nikhef.nl
†jan.steinhoff@aei.mpg.de; http://jan-steinhoff.de/physics/
‡t.p.hinderer@uu.nl

tidal fields can be decomposed into gravitoelectric and gravitomagnetic fields depending on their parity properties. The former are familiar from Newtonian gravity and involved in the dominant tidal effects due to the fundamental modes of the NS. The fundamental modes have the strongest tidal couplings and relatively high resonance frequencies, which results in their excitation remaining nonresonant for most of a quasicircular inspiral [21–23]. By contrast, gravitomagnetic tidal fields associated with relativistic frame-dragging effects lead to the excitation of inertial modes of NSs whose frequencies are proportional to the spin [24–28] and will thus invariably pass through tidal resonances in binary inspirals. The resonant energy and angular momentum transfer between the modes, orbit, and GWs leads to comparatively sudden changes in the GW frequency evolution, thus contributing a small but distinctive feature to the signals.

There has been much previous work on gravitomagnetic modes of NSs, which are associated with the Coriolis effect and include inertial modes such as the "r modes" [29–32]. Flanagan and Racine [33] computed the direct effects of the resonance on the dynamics and developed an effective waveform model for the resulting GW imprints. This model was recently revisited to assess the impact for measuring tidal deformabilities with next-generation detectors [34–36]; see [37] for use of the model for other classes of modes and [38] for studies of inertial modes in postmerger GWs. Previous studies have also modeled and examined the effect of nonresonant gravitomagnetic tides on the inferred tidal deformability [39] and included them in an effective one body model [40]. However, the conclusions were limited due to an interesting feature of the response of NS matter and spacetime to a gravitomagnetic tidal perturbation: it is characterized by two kinds of gravitomagnetic tidal deformabilities depending on the assumptions on the state of the perturbed fluid [41–46]. As shown in [47], both play a role for GWs as different linear combinations of both tidal deformabilities characterize the asymptotic limits of the tidal response of the NS before and after a gravitomagnetic mode resonance.

In this paper, we first derive an explicit expression for the effective gravitomagnetic response function characterizing the ratio of the induced current quadrupole moment to the gravitomagnetic tidal field. We specialize to a binary system at large separation with arbitrary spin orientations and low spin magnitudes. The asymptotic limits of the effective response before and after resonance yield the relevant combinations of the gravitomagnetic tidal deformabilities or Love numbers in the different adiabatic regimes far from resonances. A new aspect in this paper is that we include these effects together with the direct resonance-induced changes in the GWs from [33,34]. These previous studies further adopted a Newtonian description of NSs to compute the GW signatures. Here, we instead map all equation-of-state-dependent parameters that appear in the resonance expressions (tidal couplings and resonance frequencies of the modes) to their fully relativistic counterparts. In general, multiple quadrupolar gravitomagnetic modes with azimuthal number $|m| = 1, 2$ are resonantly excited in an inspiral, however, within our approximations, certain spin orientations favor the excitation of only one of such subclass [33], which we exploit to simplify our exploratory study. We also make use of previous findings that, for NSs, the equation-of-state information contained in gravitomagnetic Love numbers can be approximately related to the gravitoelectric tidal deformability parameter Λ, which reduces the number of signal parameters [39,48]. Furthermore, as the full parameter estimation in the entire parameter space for binary NS signals in third-generation detectors is extremely computationally expensive, we focus most of the analyses on a four-dimensional subspace and consider only a few case studies. While all of these assumptions are restrictive, our aim is to scope out the importance of gravitomagnetic modes for GW measurements with third-generation detectors using a more realistic model of these effects than in related previous studies. We first estimate the plausible changes in the width of the posterior distributions when using Bayesian data analysis with Markov chain Monte Carlo pipelines versus the Fisher matrix analysis, perform a number of sanity checks on the results, and compare with previous work. We then study the impact of different mode resonances and the asymptotic adiabatic contributions on the accuracy with which tidal deformability can be measured, as well as the biases incurred when neglecting the gravitomagnetic effects.

The paper is organized as follows. In Sec. II we obtain the effective Love number and discuss its features and the description of gravitomagnetic tidal effects far from resonance. In Sec. III we incorporate these results into a frequency-domain waveform model. We discuss the data analysis framework in Sec. IV and the results in Sec. V. Section VII contains our conclusions and outlook.

Unless otherwise specified, we use geometric units $G = c = 1$. We use capital Latin letters from the middle of the alphabet $I, J, K, \ldots$ to denote spatial components of a tensor expressed in the rest frame of a NS. These indices are raised and lowered with the flat Cartesian three-metric δ_{IJ}, thus, their up or down placement has no meaning. We use the Einstein summation convention that repeated indices are implied to be summed over. We also use round brackets around indices to denote their symmetrization, for instance, for two vectors x^I and v^J we denote $x^{(I}v^{J)} = (x^I v^J + x^J v^I)/2$.

II. EFFECTIVE GRAVITOMAGNETIC LOVE NUMBER

In this section, we review the identification of an effective Love number based on a general relativistic formalism for slowly rotating bodies to linear order in the spin [47]. We calculate an explicit expression for the

Love number using the leading-order gravitomagnetic tidal fields in a binary system. We also derive the corresponding adiabatic limits for arbitrary spin orientations by performing an orbit average. Our results focus on the quadrupole which is expected to give the largest effect and makes use of different approximation schemes adapted to the hierarchy of length scales and timescales in a binary inspiral, as explained in [47].

A. Definition of gravitomagnetic Love numbers

A NS immersed in an external gravitomagnetic tidal field B_{IJ} will develop an induced flux quadrupole moment $\mathcal{J}_{IJ}$. The gravitomagnetic quadrupolar Love number, which we denote by σ, is defined as the ratio

$$\sigma = \frac{1}{2}\frac{\mathcal{J}^{IJ}}{B^{IJ}}. \tag{2.1a}$$

Alternatively, σ can be identified as the coupling coefficient in the Lagrangian [47] describing gravitomagnetic tides in the adiabatic limit according to the conventions

$$L^{\mathcal{B}}_{\rm ad} = \frac{2\sigma}{3} B_{IJ}B^{IJ}. \tag{2.1b}$$

Calculations of magnetic Love numbers based on relativistic perturbations of a NS revealed that magnetic quadrupolar Love numbers σ can be of two types [41–46]: assuming that, under perturbations, the fluid of a nonrotating NS remains static leads to the static Love number $\sigma_{\rm stat}$, while assuming it to be irrotational yields a different result $\sigma_{\rm irrot}$. As discussed in [47] and below, both Love numbers are relevant for characterizing the gravitomagnetic tidal response of a NS asymptotically far from a mode resonance.

1. Effective frequency-dependent Love number

When going beyond the restriction to adiabatic limits, the tidal deformability generalizes to an effective frequency-dependent response function. Its particular form is obtained by considering the dynamics of the matter contributions to the flux quadrupole moment $Q^{IJ}_{\mathcal{B}}$ described by the Lagrangian given in Eq. (3.17) of [47] as

$$L^{\mathcal{B}} \approx -\frac{3}{32(\sigma_{\rm irrot}-\sigma_{\rm stat})}\left[\dot{Q}^{IJ}_{\mathcal{B}}\dot{Q}^{IJ}_{\mathcal{B}} - 2\hat{\omega}^{\mathcal{B}}\Omega^{JK}\dot{Q}^{IJ}_{\mathcal{B}}Q^{KI}_{\mathcal{B}}\right] - \frac{1}{2}B_{IJ}\dot{Q}^{IJ}_{\mathcal{B}} + \frac{2\sigma_{\rm stat}}{3}B_{IJ}B_{IJ}. \tag{2.2}$$

Here, overdots denote proper time derivatives and the tensor Ω_{IJ} is related to the NS's spin frequency $\mathbf{\Omega}$ by

$$\Omega_{IJ} = \epsilon_{IJK}\Omega^K, \tag{2.3}$$

where ϵ_{IJK} is the Levi-Civita permutation tensor. The dimensionless frequency quantity $\hat{\omega}_{\mathcal{B}}$ is given in terms of the quadrupolar gravitomagnetic mode frequencies in the corotating frame $\omega^{\mathcal{B}}_{2m}$, where $l=2$ denotes the quadrupolar modes and m the azimuthal mode number, by

$$\hat{\omega}^{\mathcal{B}} = \frac{\omega^{\mathcal{B}}_{2m}}{m\Omega}. \tag{2.4}$$

In the Newtonian limit, the mode frequencies $\omega^{\mathcal{B}}_{2m}$ reduce to $\omega^{\rm Newt}_{2m} = -m\Omega/3$ in this frame, making (2.4) independent of m.

To obtain an effective adiabatic Lagrangian in the form of (2.1) we integrate the first term in (2.2) by parts and neglect the total time derivative. We then eliminate the acceleration $\ddot{Q}^{IJ}_{\mathcal{B}}$ by using the oscillator equations of motion

$$\ddot{Q}^{IJ}_{\mathcal{B}} - 2\hat{\omega}^{\mathcal{B}}\Omega^{K(I}\dot{Q}^{J)K}_{\mathcal{B}} = \frac{8}{3}(\sigma_{\rm irrot}-\sigma_{\rm stat})\dot{B}_{IJ}. \tag{2.5}$$

Substituting these equations of motion (2.5) for $\ddot{Q}^{IJ}_{\mathcal{B}}$ into the Lagrangian and omitting total derivatives leads to

$$\bar{L}^{\mathcal{B}} \approx -\frac{1}{4}B_{IJ}\dot{Q}^{IJ}_{\mathcal{B}} + \frac{2\sigma_{\rm stat}}{3}B_{IJ}B_{IJ}, \tag{2.6}$$

which is only valid for configurations of the system that satisfy the equations of motion (2.5).

We identify the effective response function by requiring that the Lagrangian (2.6) take the form of the adiabatic Lagrangian (2.1) with σ replaced by an effective Love number

$$\bar{L}^{\mathcal{B}} \overset{!}{=} \frac{2\sigma_{\rm eff}}{3}B_{IJ}B_{IJ}. \tag{2.7}$$

Omitting total derivatives, this leads to the identification of an instantaneous (inst) effective Love number

$$\sigma^{\rm inst}_{\rm eff} = \frac{-\frac{3}{8}B_{IJ}\dot{Q}^{IJ}_{\mathcal{B}} + \sigma_{\rm stat}B_{IJ}B_{IJ}}{B_{KL}B_{KL}}. \tag{2.8}$$

This result for an effective Love number still has undesirable features, for instance, it varies over an orbit and the definition is not unique due to the different ways of assigning the time derivatives up to total derivative terms. For example, the first term in the numerator of (2.8) could equivalently be written as $3\dot{B}_{IJ}Q^{IJ}_{\mathcal{B}}/8$. These subtleties disappear when we impose that the above definitions hold only at the level of the orbit-averaged Lagrangians. Denoting the orbit average by angular brackets, we define the effective Love number by

$$\sigma_{\rm eff} = \sigma_{\rm stat} - \frac{3}{8}\frac{\langle B_{IJ}\dot{Q}^{IJ}_{\mathcal{B}}\rangle}{\langle B_{IJ}B_{IJ}\rangle}, \tag{2.9}$$

with $\dot{Q}^{IJ}_{\mathcal{B}}$ a solution to the equations of motion (2.5). This is effectively an expansion in the ratio of orbital and radiation-reaction timescales. The approximation becomes less accurate in the later inspiral: for an example of two neutron stars at (10, 1 kHz) GW frequency, the corrections are of order $\sim(10^{-8}, 10^{-2})$. This is sufficient for our purposes here to scope out the consequences for measurements; we plan to develop a refined model in future work. The above definition of the effective Love number (2.9) becomes more transparent when expressed in terms of the flux quadrupole defined in (2.1) which, as discussed in [47], is given by $\mathcal{J}^{IJ} = 2\sigma_{\rm stat}B_{IJ} - 3\dot{Q}^{IJ}_{\mathcal{B}}/4$. With this,

$$\sigma_{\rm eff} = \frac{1}{2}\frac{\langle B_{IJ}\mathcal{J}^{IJ}\rangle}{\langle B_{IJ}B_{IJ}\rangle}, \tag{2.10}$$

which is directly analogous to the definition in the gravitoelectric case.

B. Application to a binary system

To obtain an explicit expression for the effective Love number requires specifying the relevant tidal field B_{IJ}. Here, we consider a binary system composed of the NS with mass M_1 and a point-mass companion M_2 at large orbital separation. We work in the center of mass frame of the NS and introduce a coordinate system in which the position of the center of mass of the companion is $\boldsymbol{z}(t)$ and its velocity is $\dot{\boldsymbol{z}}(t)$. The gravitomagnetic tidal field B_{ij} due to the companion is then given to the leading post-Newtonian order by [33]

$$B_{ij} = \frac{6M_2}{r^5} z_{(i}\epsilon_{j)kl} z_k \dot{z}_l, \tag{2.11}$$

where r is the relative separation and we use lowercase latin indices for the spatial components of tensors in this frame.

We further specialize to quasicircular orbits of constant radius $\dot{r} = \ddot{r} = 0$ and parametrize the orbit using two angles: the azimuthal orbital phase ϕ and the inclination angle ψ of the spin axis of the NS relative to the orbital angular momentum such that the position vector becomes

$$\boldsymbol{z}(t) = r(\cos\psi\cos\phi(t), \sin\phi(t), \sin\psi\cos\phi(t)). \tag{2.12}$$

The spin inclination angle ψ is often approximated as constant because its change is very small [34,49]. The transformation of (2.11) from the NS's center of mass frame to the corotating frame is given by

$$B_{IJ} = R^i_I R^j_J B_{ij}, \tag{2.13}$$

where R^i_I are rotation matrices. We assume that the NS's spin is along the z axis in the corotating frame such that $\boldsymbol{\Omega} = (0,0,\Omega)$ and $R^1_1 = R^2_2 = \cos(\Omega t)$, $R^2_1 = \sin(\Omega t) = -R^1_2$, $R^3_3 = 1$ with all other components vanishing. The body label 1 on Ω is implied here. To reduce (2.9) to a function of the orbital parameters also requires the steady-state solution of the oscillator equations of motion (2.5). This is most conveniently calculated in a spherical-harmonic basis, using that

$$Q^{IJ}_{\mathcal{B}} = N_2 \sum_m \mathcal{Y}^{2m}_{IJ} Q^{\mathcal{B}}_m, \tag{2.14}$$

where $N_2 = \sqrt{8\pi/15}$ and $\mathcal{Y}^{2m}_{IJ}$ are symmetric-trace-free tensors whose components are complex numbers [50]. We use a similar decomposition as (2.14) for B_{IJ}. The equations of motion (2.5) can then be expressed as

$$\ddot{Q}^{\mathcal{B}}_m + im\Omega\hat{\omega}^{\mathcal{B}}\dot{Q}^{\mathcal{B}}_m = -\frac{8}{3}(\sigma_{\rm irrot} - \sigma_{\rm stat})\dot{B}_m. \tag{2.15}$$

In order to solve (2.15) for the case of interest here, we extract from (2.11)–(2.13) the spherical-harmonic components

$$B_m = N_2 \mathcal{Y}^{*2m}_{IJ} B_{IJ}, \tag{2.16}$$

where the asterisk denotes complex conjugation. For circular orbits, these coefficients are given by

$$2B_2 e^{-2i\Omega t} = \bar{\mathcal{B}}(2i\sin\psi\sin\phi - \sin 2\psi\cos\phi), \tag{2.17a}$$

$$B_1 e^{-i\Omega t} = \bar{\mathcal{B}}(i\cos\psi\sin\phi - \cos 2\psi\cos\phi), \tag{2.17b}$$

$$B_0 = \bar{\mathcal{B}}\sqrt{3/2}\cos\phi\sin 2\psi, \tag{2.17c}$$

with

$$\bar{\mathcal{B}} = \frac{3M_2\omega}{r^2}, \qquad \omega = \dot{\phi}. \tag{2.17d}$$

The results for negative m are obtained from the relation

$$B_{-m} = (-1)^m B^*_m. \tag{2.18}$$

Using these forcing terms in the equations of motion (2.15) and solving for steady-state solutions for $Q^{\mathcal{B}}_m$ leads to

$$Q_2 e^{-2i\Omega t} = \frac{8\bar{\mathcal{B}}(\sigma_{\rm irrot} - \sigma_{\rm stat})}{3D_2}[i\mathcal{A}_{2,s}c_\phi + C_{2,s}s_\phi], \tag{2.19a}$$

$$Q_1 e^{-i\Omega t} = \frac{8\bar{\mathcal{B}}(\sigma_{\rm irrot} - \sigma_{\rm stat})}{3D_1}[i\mathcal{A}_{1,c}c_\phi + C_{1,c}s_\phi], \tag{2.19b}$$

$$Q_0 = -4\sqrt{6}\frac{M_2(\sigma_{\rm irrot} - \sigma_{\rm stat})}{r^2}\sin 2\psi\sin\phi, \tag{2.19c}$$

where $c_\phi = \cos(\phi)$, $s_\phi = \sin(\phi)$, and

$$\mathcal{A}_{m,s} = \omega \sin\psi + (1+\hat{\omega}^{\mathcal{B}})\Omega \sin 2\psi, \tag{2.19d}$$

$$C_{m,s} = m\Omega(1+\hat{\omega}^{\mathcal{B}}) \sin\psi + \frac{\omega}{m} \sin 2\psi, \tag{2.19e}$$

with the corresponding quantities with subscripts c obtained by replacing "sin" by "cos" in the above expressions. The denominators in (2.19) are given by

$$D_m = \left[\omega - m\Omega(1+\hat{\omega}^{\mathcal{B}})\right]\left[\omega + m\Omega(1+\hat{\omega}^{\mathcal{B}})\right]. \tag{2.19f}$$

The final step is to use these results to obtain the effective Love number. The relevant tensor contractions entering (2.9) are given by

$$B_{IJ}B^{IJ} = 2\bar{\mathcal{B}}^2, \qquad \dot{Q}_{IJ}B^{IJ} = \sum_{m=-2}^{2} \dot{Q}_m B_{-m}. \tag{2.20}$$

Using (2.20) in (2.9) leads to the instantaneous effective Love number. Performing an orbit average for the case considered here amounts to

$$\sigma_{\rm eff} = \sigma_{\rm stat} - \frac{3}{16\bar{\mathcal{B}}^2}\frac{\omega}{2\pi}\int_0^{2\pi/\omega} \sum_{m=-2}^{2} \dot{Q}_m B_{-m} dt. \tag{2.21}$$

Substituting (2.17a) and (2.19) into (2.21) leads to the final result for the effective Love number for one of the bodies,

$$\begin{aligned}\sigma_{\rm eff} = \sigma_{\rm stat} &+ \frac{3(\sigma_{\rm irrot}-\sigma_{\rm stat})}{8}(\sin 2\psi)^2 + \frac{(\sigma_{\rm irrot}-\sigma_{\rm stat})}{2D_1}\left\{\omega\Omega\hat{\omega}^{\mathcal{B}}(\cos\psi + \cos 3\psi) + \left[\omega^2 - \Omega^2(1+\hat{\omega}^{\mathcal{B}})\right](1+\cos\psi\cos 3\psi)\right\} \\ &+ \frac{(\sigma_{\rm irrot}-\sigma_{\rm stat})(\sin\psi)^2}{4D_2}\left[8\omega\Omega\hat{\omega}^{\mathcal{B}}\cos\psi + \left(\omega^2 - 4\Omega^2(1+\hat{\omega}^{\mathcal{B}})\right)(3+\cos 2\psi)\right].\end{aligned} \tag{2.22}$$

In a binary system of two NSs, one must add the same contribution but with the parameters of the companion body.

C. Features of the effective response

1. Effects of the spin orientation

The poles of the response (2.22), i.e., where one of the factors in the denominators given in (2.19f) vanishes, correspond to the four different mode resonances for the $m \neq 0$ modes. For special cases of the spin inclination angle only a subset of the modes contributes to $\sigma_{\rm eff}$, as also evident from (2.19). For example, for aligned spin corresponding to $\psi = 0$ the response (2.22) reduces to

$$\sigma_{\rm eff}|_{\psi=0} = \sigma_{\rm stat} + \frac{(\sigma_{\rm irrot}-\sigma_{\rm stat})(\omega-\Omega)}{\omega - \Omega(1+\hat{\omega}^{\mathcal{B}})}. \tag{2.23}$$

This shows that, for aligned spins, and within our approximations, the only pole in the response is $\omega \to \Omega(1+\hat{\omega}^{\mathcal{B}})$ which corresponds to the $m=1$ resonance frequency.

Another special case is a spin inclination of $\psi = \pi/3$, where the contribution from the $|m|=1$ modes is nonresonant. This can be seen either from (2.19), by noticing that the numerator in Q_1 for this special value of ψ will involve factors of $\omega - \Omega(1+\hat{\omega}^{\mathcal{B}})$ which cancel the divergent term in the denominator, or by considering the third term in (2.22) showing the same effect.

2. Adiabatic limits

Above, we have computed the response assuming a fixed orbit, obtaining divergences in the response at the resonances. However, in a binary inspiral, the continued GW dissipation causes the system to evolve through the resonance, exciting the mode amplitudes only to a finite maximum value. This effect was already examined in detail in [33], who also developed an effective waveform model for these resonance-induced effects. A missing phenomenon from these and subsequent studies were the additional adiabatic effects due to the behavior of the modes far from the resonances. To compute the relevant NS parameters characterizing the adiabatic response, we consider the asymptotic limits of $\sigma_{\rm eff}$ long before or after a resonance. The subtleties with extracting the relevant limits were discussed in detail in [47], as the appropriate ordering of limits between $\omega, \Omega \to 0$ is delicate and depends on the situation. In particular, the relevant adiabatic limit before the mode resonance is obtained by considering $\omega \to 0$ in (2.22), while the postresonance adiabatic limit is given by taking the limit $\Omega \to 0$ first. This leads to the asymptotic expressions pre- and postresonance respectively,

$$\sigma^{\rm asym} = \begin{cases} \sigma_{\rm stat} + \frac{(\sigma_{\rm irrot}-\sigma_{\rm stat})[8+3\hat{\omega}_B \sin(2\psi)^2]}{8(1+\hat{\omega}_B)} \\ \sigma_{\rm irrot} \end{cases}. \tag{2.24}$$

We will use the above insights into the features of the response to assemble an approximate waveform model that properly accounts for both resonance and adiabatic effects.

III. EFFECTIVE WAVEFORM MODEL WITH ADIABATIC AND RESONANCE EFFECTS

A. Approximate waveform model

Computing the impact of gravitomagnetic tidal effects on the GW signals from inspiraling NS binary systems is a complicated task. Here, we bypass these challenges by assembling a simple effective model for the gravitomagnetic imprints in frequency-domain descriptions of the GW signals based on adapting existing results using the insights developed in the previous section. Such a model is very useful for scoping out the features, magnitude, and consequences of the various gravitomagnetic effects in future GW measurements and for identifying focus areas for more detailed modeling. In addition to the gravitomagnetic effects, we also include the dominant adiabatic gravitoelectric tidal effects to understand the impacts on the overall information on NS matter. We model here only the impact of tides on the GW phase of the dominant GW mode by modifying the coprecessing-frame GW phase of the IMRPhenomPv2 waveform model [51–53].

Specifically, we write the GW phasing in the frequency domain as

$$\Psi = 2\pi f t_c - \phi_c + \Psi_{\rm pm} + \Psi^{\rm tidal}_{\rm ad} + \Psi^{\rm tidal}_{\rm res}, \tag{3.1a}$$

where t_c and ϕ_c are the reference time and phase and f is the GW frequency. The term $\Psi_{\rm pm}$ is the point-mass contribution, for which we use the post-Newtonian TaylorF2 results given, e.g., in Eq. (3.18) of [54]. For the adiabatic tidal contributions $\Psi^{\rm tidal}_{\rm ad}$ we use the results of [21,39,48,55–59] given by

$$\begin{aligned}\Psi^{\rm tidal}_{\rm ad} = &-b_0\tilde{\Lambda}f^{5/3} + \left(-b_1\tilde{\Lambda} + b_2\delta\tilde{\Lambda} + b_3\tilde{\Sigma}\right)f^{7/3} \\ &- b_4\hat{\Sigma}(\chi_1,\chi_2)f^{8/3} + f_2 f^{8/3} + f_3 f^3 + f_4 f^{10/3}\end{aligned} \tag{3.1b}$$

and take the resonance-induced effects from [33,34] in the form

$$\Psi^{\rm tidal}_{\rm res} = -\sum_{i=1,2}\left(1 - \frac{f}{f^{\rm res}_i}\right)|\Delta\Phi_i|\Theta(f - f^{\rm res}_i). \tag{3.1c}$$

The resonance effects included here are due to gravitomagnetic modes only, which are the focus of this work. For a more complete model, also gravitoelectric modes (in particular the f mode) should be included. We note that the signs of all the contributions made explicit here correspond to those relevant for the parameter choices for the case studies discussed in Sec. V below, with all the tidal parameters $\tilde{\Lambda}, \delta\tilde{\Lambda}, \tilde{\Sigma}, \hat{\Sigma}$ defined below being positive. We also see that the resonance contribution is a distinct sudden change in the phase and time of the GW signal at the resonance, whose scaling with the frequency is degenerate with that of the gauge parameters ϕ_c and t_c in the phasing (3.1). The various coefficients in (3.1b) are given by

$$b_0 = \frac{117(\pi M)^{5/3}}{256\nu}, \qquad b_1 = \frac{9345(\pi M)^{7/3}}{8192\nu}, \tag{3.2}$$

$$b_2 = \frac{19785(\pi M)^{7/3}}{46592\nu}\sqrt{1-4\nu}, \tag{3.3}$$

$$b_3 = \frac{3(\pi M)^{7/3}}{128\nu} = b_4/(\pi M)^{1/3}, \tag{3.4}$$

with $M = M_1 + M_2$ the total mass and $\nu = M_1M_2/M^2$. The functions f_j depend on $\tilde{\Lambda}, \delta\tilde{\Lambda}$, and for f_2 additionally on the spins $\chi_{1,2}$. In particular, the expression for the function f_2 in (3.1b) is obtained from Eqs. (7) and (9) of [60] and those for f_3, f_4 from Eq. (6.6b) of [58]. The parameters $\tilde{\Lambda}$ and $\delta\tilde{\Lambda}$ characterizing the gravitoelectric effects are given by

$$\tilde{\Lambda} = \frac{16}{13}\left(\frac{12}{X_1} - 11\right)X_1^5\Lambda_1 + (1 \leftrightarrow 2), \tag{3.5}$$

$$\begin{aligned}2\delta\tilde{\Lambda} = &\sqrt{1-4\nu}\left(1 - \frac{13272}{1319}\nu + \frac{8944}{1319}\nu^2\right)(\Lambda_1 + \Lambda_2) \\ &+ \left(1 - \frac{15910}{1319}\nu + \frac{32850}{1319}\nu^2 + \frac{3380}{1319}\nu^3\right)(\Lambda_1 - \Lambda_2),\end{aligned} \tag{3.6}$$

with Λ_i the dimensionless quadrupolar gravitoelectric tidal deformability parameters of each body indexed here by i. We also denote $X_i = M_i/M$ and $(1 \leftrightarrow 2)$ indicates the operation of adding the same terms but with the body labels interchanged. The gravitomagnetic parameters in (3.1b) are defined by [60]

$$\tilde{\Sigma} = \left(\frac{6920}{7} - \frac{20740}{21X_1}\right)X_1^5\Sigma_1 + (1 \leftrightarrow 2), \tag{3.7a}$$

$$\hat{\Sigma} = \left[\chi_1 - \left(\frac{4933}{3X_1} - \frac{9865}{3} + 1644X_1\right)\chi_2\right]X_1^5\Sigma_1 + (1 \leftrightarrow 2), \tag{3.7b}$$

with $\chi_i = S_i/M_i^2$ the dimensionless spin parameter of each body. We use for the dimensionless gravitomagnetic deformability parameters Σ_i the asymptotic results of Sec. II C 2 to replace

$$\Sigma_i = \frac{\sigma_i^{\rm asym}}{M_i^5} \tag{3.7c}$$

using the appropriate pre- or postresonance expressions from (2.24).

In the resonance contributions (3.1c), the quantity Θ denotes the Heaviside step function, and $f_i^{\rm res}$ are the GW frequencies at which the mode resonances occur. They are related to the gravitomagnetic mode frequencies $\omega_{2m}^{\mathcal{B}}$ by

$$f^{\rm res} = \frac{\omega_{2m}^{\rm inertial}}{\pi}, \tag{3.8}$$

where the mode frequencies in the inertial frame can be obtained by shifting

$$\omega_{2m}^{\rm inertial} = \omega_{2m}^{\mathcal{B}} - m\Omega. \tag{3.9}$$

The quantities $\Delta\Phi_{1,2}$ are the corresponding resonance-induced phase shifts, which, for the $l = 2$ modes with $m = 2$ and $m = 1$, are given by [33]

$$\Delta\Phi_{2m} = -\frac{10\pi^2}{192}\left(\frac{2m}{3}\right)^{2/3}(M_i\Omega_i)^{2/3}\left(\frac{M_i}{\mathcal{M}}\right)^{10/3}\mathcal{I}_i^{2m}, \tag{3.10a}$$

where $\mathcal{M} = (M_1M_2)^{3/5}/M^{1/5}$ is the chirp mass and

$$\mathcal{I}_i^{22} = (\bar{I}_i^r)^2\sin^2(\psi_i)\cos^4\left(\frac{\psi_i}{2}\right)(1 - X_i), \tag{3.10b}$$

$$\mathcal{I}_i^{21} = (\bar{I}_i^r)^2\cos^2\left(\frac{3\psi_i}{2}\right)\cos^2\left(\frac{\psi_i}{2}\right)(1 - X_i), \tag{3.10c}$$

with $\bar{I}_i^r$ related to the dimensionless relativistic tidal deformabilities by [47]

$$(\bar{I}^r)^2 = \frac{15}{4\pi}(\Sigma_{\rm stat} - \Sigma_{\rm irrot}). \tag{3.10d}$$

B. Reducing the number of matter parameters using quasiuniversal relations

Even within the restricted context considered here, the effective GW model for the tidal signatures (3.1b) and (3.1c) contains ten matter parameters, namely the deformabilities Λ_i, $\sigma_i^{\rm stat}$, $\sigma_i^{\rm irrot}$ and resonance frequencies for the $m = 1$ and $m = 2$ modes for each body. Such a large number of extra parameters prevents the data analysis from yielding meaningful results. We reduce the number of parameters by using empirical quasiuniversal relations that are approximately independent of the equation of state and enable an approximate reduction of the matter parameters to one deformability Λ for each body. The quasiuniversal relations are of the form [39,48]

$$\ln(\mp\,\Sigma) = \sum_{n=0}^{5} a_n Y^n, \tag{3.11}$$

with the irrotational case corresponding to the minus sign and coefficients $a_n^{\rm irrot} = \{-2.03, 0.487, 0.00969, 0.00103, 9.37\times10^{-5}, 2.24\times10^{-6}\}$, while the plus sign applies for the static case with $a_n^{\rm stat} = \{-2.66, 0.786, -0.01, 0.00128, -6.37\times10^{-5}, 1.18\times10^{-6}\}$ and where

$$Y = \ln(\Lambda). \tag{3.12}$$

The GW frequencies appearing in the resonant mode contributions (3.1c) are given by (3.8), which can be written explicitly as

$$f^{\rm res} = \frac{1}{\pi}(\kappa_m - m)\Omega, \tag{3.13}$$

where the parameter κ_m reduces to $\kappa_m \to 2m/3$ in the Newtonian limit, while for relativistic stars, it is approximately related to Λ by [26,61]

$$\kappa_2 = 0.3668 + 0.0498Y - 0.0025Y^2. \tag{3.14}$$

We note that these results from [26] are specialized to the $m = 2$ mode. Within the effective action model (2.2) we are using, the modes with different m all have the same scaled frequency $\hat{\omega}_{\mathcal{B}}$ and hence the same κ. Thus, we use (3.14) also for the $m = 1$ modes.

With the GW phasing model for the gravitomagnetic effects in hand, we next apply it in a data analysis framework to study the impact on GW measurements.

IV. ANALYSIS FRAMEWORK

A Bayesian data analysis framework is commonly used for GW signals, as explained, e.g., in [13] and briefly reviewed below. We assume that, in the absence of any GW signal, the detector noise n has a Gaussian distribution, where louder noise realizations are less likely. In the presence of a signal h with parameters $\boldsymbol{\theta}$, the data d from the detector output can be decomposed as

$$d = h(\boldsymbol{\theta}) + n, \tag{4.1}$$

for some noise realization n. Then, the likelihood $\mathcal{L}$ for the detector to measure the data d for a signal with parameters $\boldsymbol{\theta}$ is given by

$$\log\mathcal{L}(d|\boldsymbol{\theta}) = -\frac{1}{2}(d - h(\boldsymbol{\theta})|d - h(\boldsymbol{\theta})). \tag{4.2}$$

Here, the meaning of $(.|.)$ differs on both sides of the equation: on the left-hand side, $\mathcal{L}(d|\boldsymbol{\theta})$ denotes the conditional probability of observing the data d for a collection of signal parameters $\boldsymbol{\theta}$, while on the right-hand side, the notation $(.|.)$ indicates an inner product on the vector space

of signals. For two signals h_1 and h_2 this inner product is defined as

$$(h_1|h_2) = 4\mathcal{R}\int_{f_{\rm low}}^{f_{\rm high}} \frac{\tilde{h}_1(f)^* \tilde{h}_2(f)}{S_n(f)}\, df. \tag{4.3}$$

The symbol $\mathcal{R}$ denotes the operation of taking the real part, the integration limits are the lower and upper frequency range considered, S_n is the noise spectral density of the detector, and the tilde and asterisk indicate the Fourier transform and complex conjugate respectively. This log likelihood (4.2) can be further expanded as

$$\log \mathcal{L}(d|\boldsymbol{\theta}) = -\frac{1}{2}[(d|d) + (h(\boldsymbol{\theta})|h(\boldsymbol{\theta})) - 2(d|h(\boldsymbol{\theta}))]. \tag{4.4}$$

The first term is proportional to the log noise evidence and the second term $(h(\boldsymbol{\theta})|h(\boldsymbol{\theta})) = \rho^2_{\rm opt}$ is called the optimal matched filter signal-to-noise ratio (SNR) squared. The third term is the product of the optimal SNR and the matched filter SNR given by $(d|h(\boldsymbol{\theta})) = \rho_{\rm opt}\rho_{\rm mf}$.

The posterior probability distribution of the parameters $\boldsymbol{\theta}$ follows from the Bayes theorem,

$$p(\boldsymbol{\theta}|\mathcal{H}, d, \mathcal{I}) = \frac{p(d|\mathcal{H}, \boldsymbol{\theta}, \mathcal{I}) p(\boldsymbol{\theta}|\mathcal{H}, \mathcal{I})}{p(d|\mathcal{H}, \mathcal{I})}, \tag{4.5}$$

where $\mathcal{I}$ is the background information, and $\mathcal{H}$ is the hypothesis, i.e., the waveform model. The quantity $p(\boldsymbol{\theta}|\mathcal{H}, \mathcal{I})$ is the prior probability, i.e., knowledge about the parameters within the model before analyzing the data, $p(d|\mathcal{H}, \mathcal{I})$ is the evidence, and $p(d|\mathcal{H}, \boldsymbol{\theta}, \mathcal{I})$ is the likelihood function which is identified with (4.4). Computing the posterior probability distribution of the parameters $\boldsymbol{\theta}$ requires Markov chain Monte Carlo (MCMC) samplers [62].

The above framework is general but also computationally intensive, especially when taking into account the following considerations. Gravitomagnetic tidal effects are subdominant as shown in Fig. 1 [33,39], though expected to be relevant for next-generation GW detectors. The detectors will have a much wider frequency band than current detectors such that signals from NS binaries will linger for many hours to days within the sensitive band. The associated tremendous computational costs severely limit the scope of explorative studies possible with the current MCMC code infrastructures. However, "golden" events similar to GW170817, which would have a SNR of over a thousand in next-generation detectors, will provide rich science yields, especially when combined with the larger number of events with lower SNR. For the exploratory studies in this paper, we use an MCMC analysis in a lower-dimensional subspace of the signal parameters, which we validate against a simplified data analysis framework based on approximations for large SNR: the Fisher matrix

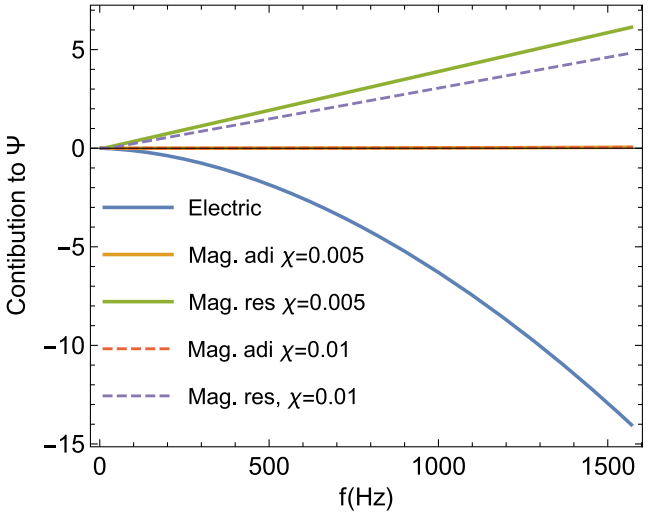

FIG. 1. Phase accumulation due to tidal effects described in (3.1b) and (3.1c). The plot shows phase accumulation due to adiabatic electric tidal effects (blue curve), adiabatic magnetic tidal effects (orange and red curve), and resonant magnetic tidal effects (green and violet curve) as a function of frequency for aligned spins $\chi = \{0.005 \text{ and } 0.01\}$ with masses $(M_1, M_2) = (1.5, 1.3)M_\odot$ and tidal deformability parameters $(\tilde{\Lambda}, \delta\tilde{\Lambda}) = (519.38, 48.37)$. The terms "Electric," "Mag. adi" and "Mag. res" denotes adiabatic gravitoelectric tidal contribution in (3.1b), adiabatic gravitomagnetic tidal contribution in (3.1b) and resonant gravitomagnetic tidal contribution in (3.1c) respectively.

formalism. For a high SNR event and Gaussian noise, the probability distributions of the best-fit parameters will be Gaussians centered around the actual values. Let $\boldsymbol{\theta}$ be the true value of the parameters and $\boldsymbol{\theta} + \boldsymbol{\Delta\theta}$ the best-fit parameters in the presence of Gaussian noise. Then for large SNR, the likelihood function is given by

$$p(\boldsymbol{\Delta\theta}) = \mathcal{N} e^{-\frac{1}{2}\Gamma_{ij}\Delta\theta^i\Delta\theta^j}, \tag{4.6}$$

where the Fisher matrix Γ_{ij} is defined as

$$\Gamma_{ij} = \left(\frac{\partial h}{\partial\theta^i}\middle|\frac{\partial h}{\partial\theta^j}\right). \tag{4.7}$$

The 1-σ error σ^i on the parameters θ^i is then given by

$$\sigma^i = \sqrt{(\Gamma^{-1})^{ii}}. \tag{4.8}$$

V. RESULTS

We use the analysis frameworks described in Sec. IV to analyze the impact of gravitomagnetic tides on the measurability of the tidal Love number Λ. For simplicity, we focus on the Cosmic Explorer (CE) detector [63], however, we expect similar results for the Einstein Telescope [8].

A. Setup and parameter choices for case studies

We consider a few illustrative cases for our analysis. These examples represent only a small subset of the expected range of diverse events but nevertheless yield useful insights. Specifically, we consider binary neutron stars with masses $(M_1, M_2) = (1.5, 1.3)M_\odot$ and explore two values of the dimensionless spin parameters $\chi = 0.005$ and $\chi = 0.01$ for each NS, where χ refers to the spin magnitudes. For the tidal deformability parameters we choose $(\tilde{\Lambda}, \delta\tilde{\Lambda}) = (519, 48)$, corresponding to the MPA1 equation of state. The choice of masses and tidal deformability parameters of binary neutron stars are compatible with the observed binary neutron star GW170817 source [1,64]. We use quasiuniversal relations [65] between the moment of inertia and Λ to convert from χ to the spin frequency Ω. In general, both the $m = 1$ and $m = 2$ resonances will contribute to the signals. To isolate each of these resonance effects and analyze its contributions, we choose spin inclination angles of $\psi = 0$ (aligned spins) and $\psi = \pi/3$ such that only the $m = 1$ or $m = 2$ modes, respectively, undergo a resonant excitation within our approximations. We assume the same spin magnitudes and orientations for both NSs.

We analyze the signals in the CE detector sensitivity [63] between $f_{\rm low} = 5$ and $f_{\rm high} \sim 1720$ Hz, which is a proxy for the merger frequency based on the estimates for nonspinning NSs from [66]. Unless otherwise specified, the SNR for the signals from these systems is 1800 for the CE detector, which corresponds to an event similar to GW170817.

For the above choices of binary parameters, the mode resonance frequencies for the larger and smaller mass NSs are given by $f_1^{\rm res} = 12$ (24) and $f_2^{\rm res} = 13$ (26) Hz for the $m = 1$ ($m = 2$) modes, respectively, and taking the spin magnitudes to be $\chi = 0.005$; they increase to twice these numbers when doubling the spin magnitudes to $\chi = 0.01$. Figure 2 illustrates the location of these resonances together with the power spectral density of the CE detector [63].

To study the consequences of different effects, we consider different tidal waveform models. We refer to the "PNTidal" model as the piece of (3.1b) involving only the adiabatic gravitoelectric tidal effects characterized by $\tilde{\Lambda}, \delta\tilde{\Lambda}$; we denote models that also include gravitomagnetic effects by PNTidal$^{\rm modes}$ for the resonant contributions (3.1c), PNTidal$_{\rm asym}$ for the asymptotic adiabatic contributions, and PNTidal$^{\rm modes}_{\rm asym}$ for the model which includes all gravitomagnetic effects. Because we work only to linear order in the spins, we neglect the effects of spin-induced multipole moments on the GWs. We have modified the tidal contribution to the phase in the IMRPhenomPv2 waveform in LALSuite to obtain the above waveform models [67]. For Bayesian parameter estimation, we use PyCBC to call different waveform models from LALSuite, generate the power spectral density curve, and construct the likelihood function (4.2) [68]. From this likelihood function we obtain the posterior distribution of parameters using the EMCEE sampler [62].

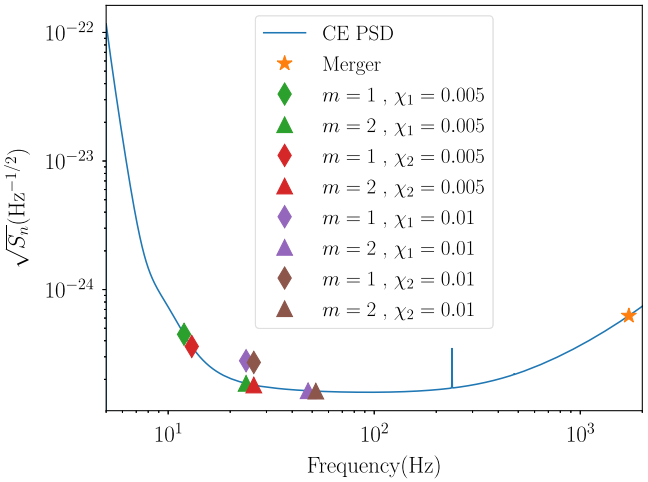

FIG. 2. CE noise spectral density and various mode resonances for the two bodies and varying spins χ. Green and purple symbols refer to the NS with mass $M_1 = 1.5M_\odot$ with lower and higher spin respectively, while red and brown symbols are the corresponding values for the companion of mass $M_2 = 1.3M_\odot$. Diamond shapes denote the modes with azimuthal number $m = 1$, triangles those with $m = 2$. Note that the y value of the symbols has no meaning.

B. Consistency checks

1. Fisher matrix versus Bayesian parameter estimation and effect of the dimensionality of the parameter space

The Fisher matrix approximation is valid for high SNR, which we expect to hold for most of the case studies considered here. To assess the validity of this expectation we compare with Bayesian parameter estimation results for the case of the PNTidal matter model. In principle, the waveforms are characterized by 17 parameters, after reducing the matter parameters to just Λ for each body. Exploring the full parameter space is thus very computationally expensive. For efficiency, we focus the comparative analysis here only on the following restricted subset of the intrinsic parameters:

$$\theta = (t_c, \phi_c, \tilde{\Lambda}, \delta\tilde{\Lambda}), \tag{5.1}$$

and fix the other parameters to be $\psi_1 = 0$, $\psi_2 = 0$, $\chi_1 = 0.01$, and $\chi_2 = 0.01$. This subset was chosen to contain the matter-related parameters $\tilde{\Lambda}$ and $\delta\tilde{\Lambda}$ as well as t_c and ϕ_c which are degenerate with mode resonance effects. We calculate the Fisher matrix (4.7) analytically and sample the Fisher likelihood (4.6) with the uniform prior on all parameters as well as constraints $\Lambda_1 \geq 0$,

$\Lambda_2 \geq 0$. In principle, the 1-σ error for all parameters could be obtained from (4.8) using the Fisher matrix (4.7), however, for higher dimensions, the Fisher matrix is ill conditioned which makes it difficult to use (4.8), which is why sampling the Fisher likelihood is preferred. We also perform a Bayesian analysis for the same setup using the EMCEE sampler [62] to obtain the posterior probability distribution of the parameters. Figure 3 shows the results of both analyses. We see that, in this case, the results from the Fisher (blue curve) and Bayesian (orange curve) frameworks agree well and are centered on the injected value (vertical line). To obtain an estimate of the changes in the width of the posterior distributions when including more parameters, in particular the masses and spin magnitudes for each body, we also perform a Fisher analysis for eight free parameters $\boldsymbol{\theta} = (t_c, \phi_c, M_1, M_2, \tilde{\Lambda}, \delta\tilde{\Lambda}, \chi_1, \chi_2)$. More specifically, we obtain a mean and 90 percentile results of $\tilde{\Lambda} = 519^{+5.1}_{-4.7}$ from the MCMC and $\tilde{\Lambda} = 518.9^{+4.8}_{-4.9}$ from the Fisher analyses with four free parameters respectively, which shows that they are in good agreement. For an eight-dimensional parameter space we find $\tilde{\Lambda} = 518.9^{+11.3}_{-11.2}$, which indicates that when doubling the dimensionality of the parameter space the posterior distributions increase in width by about a factor of 2. The good agreement between the Fisher and Bayesian results also provides a useful check of the 4D MCMC sampling, which is the method we will continue to use in what follows.

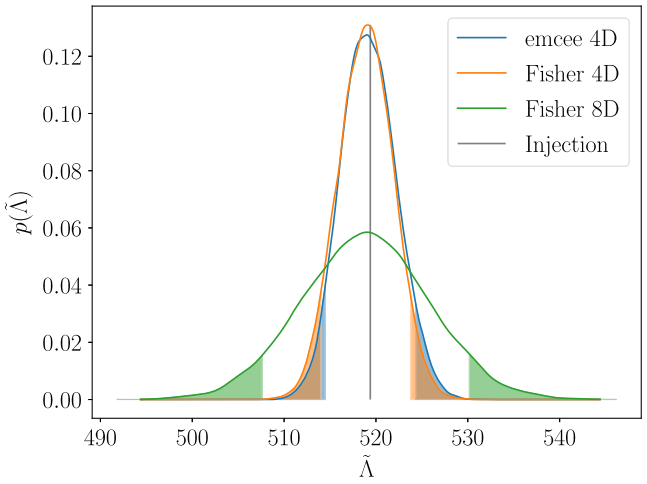

FIG. 3. Posterior probability distribution of $\tilde{\Lambda}$ for SNR 1800 with the PNTidal waveform model (without gravitomagnetic effects) used for injection and recovery. The label 4D refers to a reduced parameter space of the tidal deformabilities $\tilde{\Lambda}, \delta\tilde{\Lambda}$ and the time and phase of coalescence t_c, ϕ_c with all other parameters fixed, while 8D also includes the sampling of the mass and spin parameters for each body. The results from the Fisher matrix (orange curve) agree well with the corresponding Bayesian analysis (blue curve), with both centered on the injected value (vertical line). The green curve shows the broadening of the distribution when doubling the dimensionality of the parameter space sampled. The shaded tails of the curves indicate regions outside the 90% credible interval. For the parameter $\delta\tilde{\Lambda}$, both the 4D and 8D posteriors are essentially flat in this case.

2. Comparison to the adiabatic effects studied in [60]

The final consistency check we perform here is to compare with the results of [60] for the impact of adiabatic gravitomagnetic effects on measurements of $\tilde{\Lambda}$. Following [60] we restrict our analysis to only three free parameters $\theta = (t_c, \phi_c, \tilde{\Lambda})$, with all the other parameters fixed. Figure 4 shows the results for aligned spins of magnitude $\chi = 0.005$. Comparing the orange curve (no mode resonances) and blue curve (no adiabatic effects) to the green curve shows that in this case the largest impact of gravitomagnetic effects is due to the adiabatic limits, while mode resonances play a subdominant role. Specifically, we obtain $\tilde{\Lambda} = 519.3^{4.5}_{-4.5}$ with the full model (green curve) that was also used for the injection and thus quantifies the statistical errors. Using only the adiabatic effects (orange curve) leads to $\tilde{\Lambda} = 520.9^{4.4}_{-4.4}$, which is close to the injected value. On the other hand, including only the mode resonances for the recovery while neglecting the adiabatic effects (blue curve) leads to a distribution that is significantly shifted away from the injected value with $\tilde{\Lambda} = 515.1^{4.6}_{-4.5}$. The smallness of the effect of the mode resonances on measurements of $\tilde{\Lambda}$ is in part due to the fact that the resonance-induced phase corrections (3.1c) have a scaling in frequency degenerate with the gauge parameters t_c and ϕ_c in the phase (3.1a), which absorbs some of the resonance effects into shifts of t_c and ϕ_c. Specifically, for $f > f^{\mathrm{res}}$, the resonance-induced phase shift (3.1c) comprises a constant contribution $-|\Delta\Phi|$ and a term that grows linearly with frequency $|\Delta\Phi| f/f^{\mathrm{res}}$, where the coefficient $|\Delta\Phi|$ is given in (3.10). These constant and linear terms add to the contributions parametrized by ϕ_c and $2\pi f t_c$ respectively in the total phase (3.1a). The adiabatic effects show a similar magnitude as found in [60] based on only the irrotational or static Love numbers, which lead to shifts in the posterior distributions to lower and higher values respectively, cf. Fig. 6 therein. While the specific choices for the case study here differ from [60] the setup is similar enough to interpret qualitative trends by comparing their findings to the adiabatic results represented by the orange curve in Fig. 4, which uses the more realistic asymptotic Love numbers from (2.24) as opposed to only σ_{irrot} for the entire waveform.

C. Physical effects

Having performed the consistency checks discussed above, we next analyze the impact of various physical effects and parameter dependencies by Bayesian parameter estimation on the four-dimensional parameter space (5.1). We first consider nonspinning systems, where there is no effect from the mode resonances, then aligned spins with

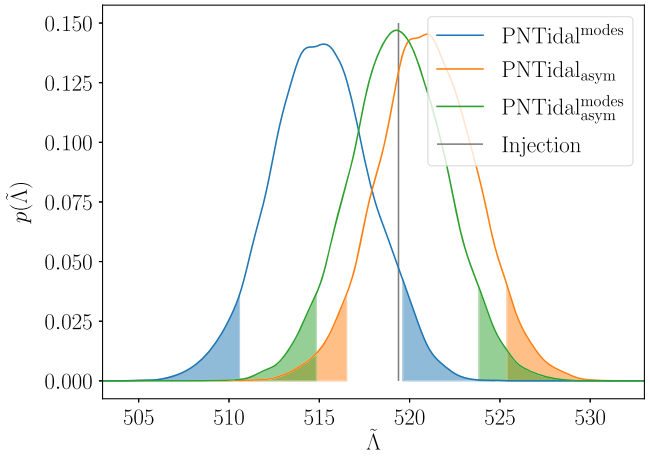

FIG. 4. Shifts in the posterior distribution for $\tilde{\Lambda}$ due to adiabatic and resonant gravitomagnetic effects. This case study is for SNR 1800, aligned spins $\chi = 0.005$, and sampling only on $(\tilde{\Lambda}, t_c, \phi_c)$ with all other parameters fixed. We inject with a waveform that includes all effects PNTidal$^{\rm modes}_{\rm asym}$ and recover with the same waveform (green curve) and those that include only the resonance jumps (blue curve) and only the adiabatic effects (orange curve). In this case the contribution from the adiabatic effects is dominant; omitting them (as for the results shown by the blue curve) leads to the largest shifts in the distribution.

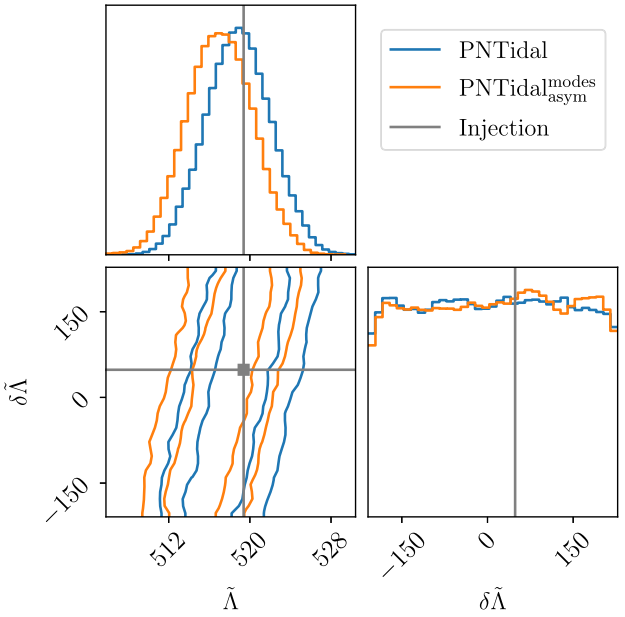

FIG. 5. Posterior distributions of the tidal parameters for nonspinning NSs at SNR 1800. The injection neglected gravitomagnetic tides, and the blue curve illustrates the recovery with the same waveform. The effect of gravitomagnetic tides, which are purely adiabatic in this case, is indicated by the orange curve. In the two-dimensional representation in the lower left panel, the contours correspond to the 1- and 2-σ confidence levels.

only the $m = 1$ modes resonant, and finally spin orientations that maximize the effects of the $m = 2$ modes.

1. Gravitomagnetic effects for nonspinning systems

For this study we use the PNTidal model without the gravitomagnetic effects as the reference baseline for the injection and set $\chi = 0$. Figure 5 shows the results for the posterior distributions in the tidal parameters $\tilde{\Lambda}$ and $\delta\tilde{\Lambda}$, with the two-dimensional representations given in the lower left panel and the one-dimensional projections for each parameter in the upper and right panels. The one-dimensional representations are the full distributions, while the contours in the $\tilde{\Lambda} - \delta\tilde{\Lambda}$ plane correspond to the credible intervals at the 1-σ (68%) and 2-σ (95%) confidence level. The blue curves in Fig. 5 represent a consistency check that when injecting and recovering with the same model the mean is centered on the injected value indicated by the gray lines and quantify the statistical uncertainties. The orange curve in Fig. 5 corresponds to the results obtained when including all gravitomagnetic effects, where, however, for nonspinning systems there is only an adiabatic gravitomagnetic effect, no resonances. As expected, we see that they induce a small shift in the posterior for $\tilde{\Lambda}$. We note that the difference to the study in Sec. V B 2 is the model used for the injection, the value of the spins, which also impacts the adiabatic gravitomagnetic parameters (3.7), and the dimensionality of the parameter space sampled. We also observe that the adiabatic effects have no significant impact on the measurability of $\delta\tilde{\Lambda}$ in this case, as the shape of the error ellipses and the flat distribution in $\delta\tilde{\Lambda}$ remain largely unaffected.

2. Effect of gravitomagnetic tides for aligned spins

A more realistic scenario is to include finite spins of the NSs. We first consider the case of aligned spins, where the $m = 1$ mode resonances contribute in addition to the adiabatic effects. As in Sec. V C 1, we use the model without gravitomagnetic tides as the reference baseline for the injection and recover with the same model (blue curve) as well as the model including all gravitomagnetic effects (orange curve). For small spins $\chi = 0.005$, we see from Fig. 6 that the gravitomagnetic effects lead to a slightly larger shift in the posterior probability distributions than in the nonspinning case shown in Fig. 5. These trends become more discernible for higher spins of $\chi = 0.01$ shown in Fig. 7. For higher spins, the recovered distributions for $\tilde{\Lambda}$ with and without gravitomagnetic effects have essentially no overlap. We also notice that compared to the low-spin case in Fig. 6 the shift in the distribution for $\tilde{\Lambda}$ is in the opposite direction. We will investigate the causes of this below in Sec. VI. Roughly, it can be attributed to the fact that for higher spins the resonances occur at higher frequency, as seen in Fig. 2. Furthermore, as also found in [34], which included only the mode resonance effects with Newtonian parameters, the presence of gravitomagnetic tides significantly improves the measurability of $\delta\tilde{\Lambda}$.

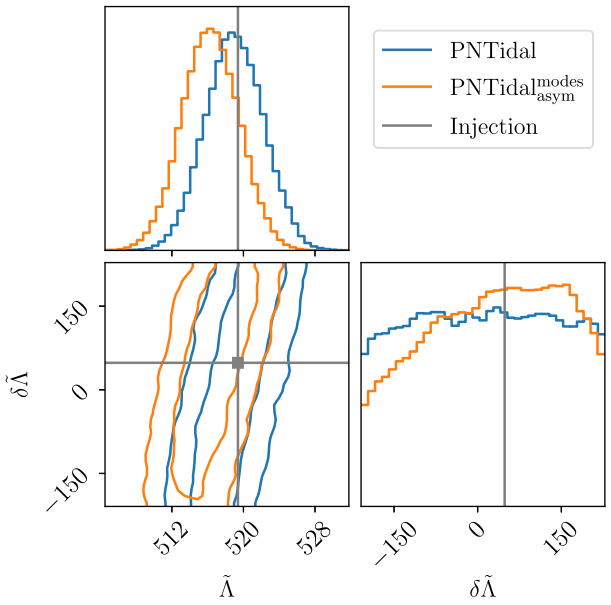

FIG. 6. Gravitomagnetic effects for aligned spins of $\chi_{1,2} = 0.005$ and SNR 1800. The blue curve corresponds to using the same waveform for injection and recovery. Comparing this with the orange curve indicates the changes due to gravitomagnetic tides from both the $m = 1$ mode resonances and the adiabatic effects, which lead to a shift in the distribution of $\tilde{\Lambda}$ and a slight change in the shape of the $\delta\tilde{\Lambda}$ posterior.

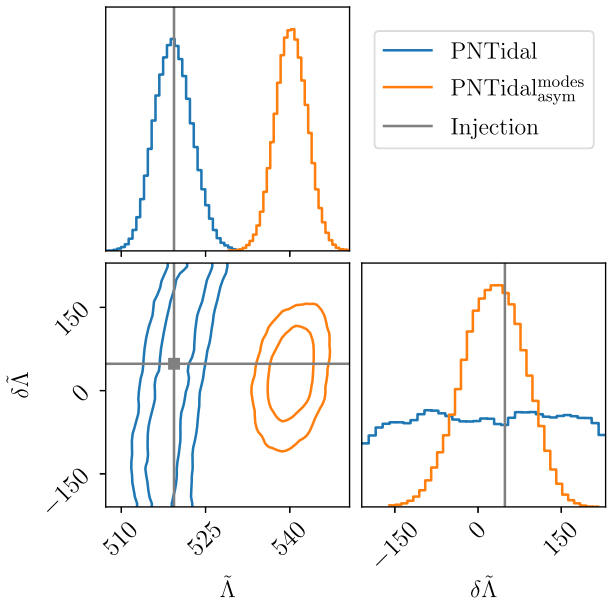

FIG. 7. Gravitomagnetic effects for aligned spins of $\chi_{1,2} = 0.01$ and SNR 1800. The blue curve corresponds to using the same waveform for injection and recovery, the orange curve indicates the effect of gravitomagnetic tides from both the $m = 1$ mode resonances and the adiabatic effects. Significant shifts in $\tilde{\Lambda}$ and a peaked shape of the distribution of $\delta\tilde{\Lambda}$ are clearly visible in this case. This is also illustrated by the two-dimensional representation of the error ellipses in the lower left panel.

This is indicated by a peak in the one-dimensional projection or the size of the ellipse in the $\tilde{\Lambda} - \delta\tilde{\Lambda}$ plane, which is in contrast to the distribution being essentially uninformative when neglecting the gravitomagnetic effects (cf. the blue curves in Fig. 7).

3. Effects of different gravitomagnetic contributions for aligned spins

Having quantified the impact of gravitomagnetic effects, we next investigate the relative importance of adiabatic and resonant contributions to these results. For this purpose, we switch to using the full tidal model PNTidal$^{\text{modes}}_{\text{asym}}$ for the injections. The results when recovering with different models that are missing various effects for the case with spins of $\chi = 0.005$ are shown in the upper panels of Fig. 8. The green curve illustrates the recovery with the same model as the injection, the blue curve corresponds to omitting the adiabatic effects, while the orange curve illustrates the omission of resonance effects from the model. From the large (small) shift away from the injected value in the distribution for $\tilde{\Lambda}$ when omitting (including) adiabatic effects it follows that the conclusions of Sec. V B 2 about the signatures from adiabatic tides dominating over the resonance effects in this case continue to hold for the larger parameter space considered here. Furthermore, we also see by comparing the orange and blue curves in the upper panels of Fig. 8 that the more peaked distribution in $\delta\tilde{\Lambda}$ can be primarily attributed to the mode resonances in this case.

The lower panel of Fig. 8 shows the same study with higher spins of $\chi = 0.01$. We see the opposite behavior compared to the case with lower spins: now the mode resonances (blue curves) dominate over adiabatic effects (orange curve) for measuring $\tilde{\Lambda}$ without bias; in fact the inferred $\tilde{\Lambda}$ with the adiabatic model has no overlap with the injected value in this case. In all cases, a peaked distribution in $\delta\tilde{\Lambda}$ emerges, indicating that it is measurable, though with significantly larger errors than $\tilde{\Lambda}$. The resonance effects yield a double-peaked distribution in this parameter for $\chi = 0.01$, which we attribute to the larger spacing of the two resonances in this case. Interestingly, for $\chi = 0.01$ the adiabatic effects contribute about equally to measuring $\delta\tilde{\Lambda}$ as the mode resonances, which is in contrast with the case of lower spins. We notice also a slight bimodality for $\chi = 0.005$ with PNTidal$^{\text{modes}}_{\text{asym}}$, which we attribute to a competition between adiabatic and resonant effects, which act in opposite directions.

4. Effect of the $m = 2$ modes

The analysis thus far focused on aligned-spin systems where only the $m = 1$ modes are resonant. In this subsection we quantify the impact of the $m = 2$ mode resonances by choosing spin orientations $\psi = \pi/3$

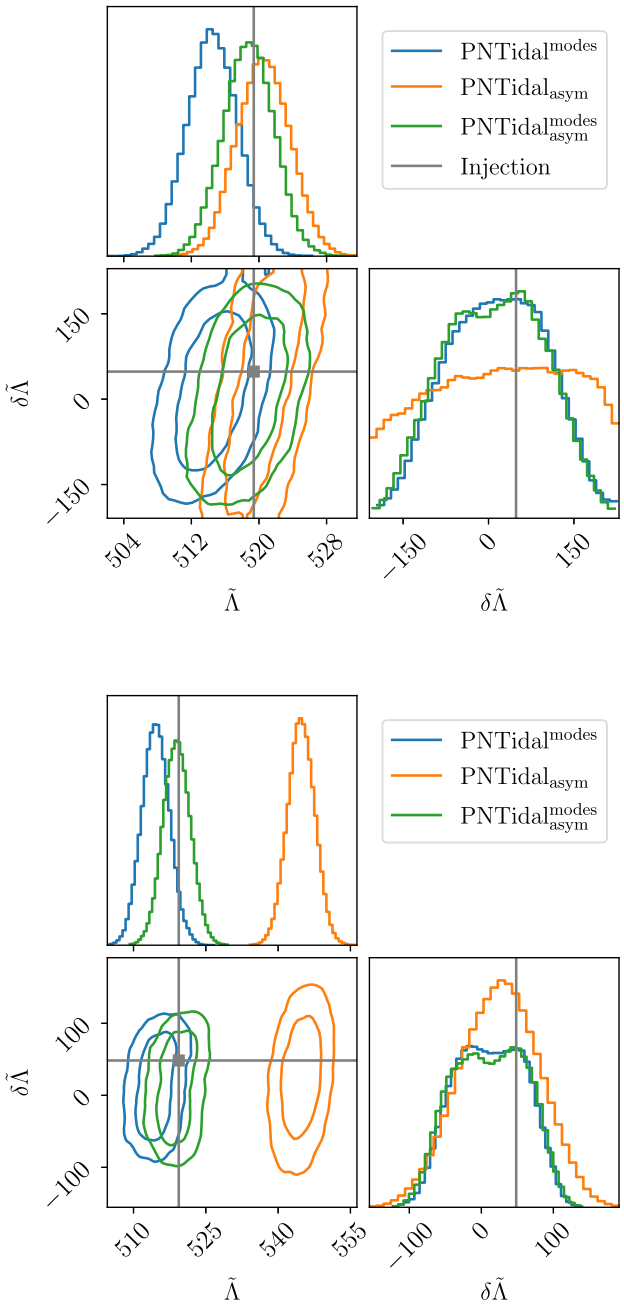

FIG. 8. Effects of various gravitomagnetic contributions on the parameter recovery for aligned spins. The results are for the systems with SNR 1800 and spins of $\chi = 0.005$ (upper) and $\chi = 0.01$ (lower). Green curves correspond to recovering with the same full model as used for the injection, blue curves include only the mode resonances, while orange curves indicate the adiabatic effects. We see that the conclusions about the impact of the resonance and adiabatic effect is opposite for the lower and higher spins: for low spins, adiabatic effects are most important for reducing the bias in $\tilde{\Lambda}$, while resonances give the dominant contribution to the measurability of $\delta\tilde{\Lambda}$. For high spins, the largest reduction in the bias in $\tilde{\Lambda}$ is due to the resonances, while the impact on $\delta\tilde{\Lambda}$ is comparable between resonance and adiabatic effects.

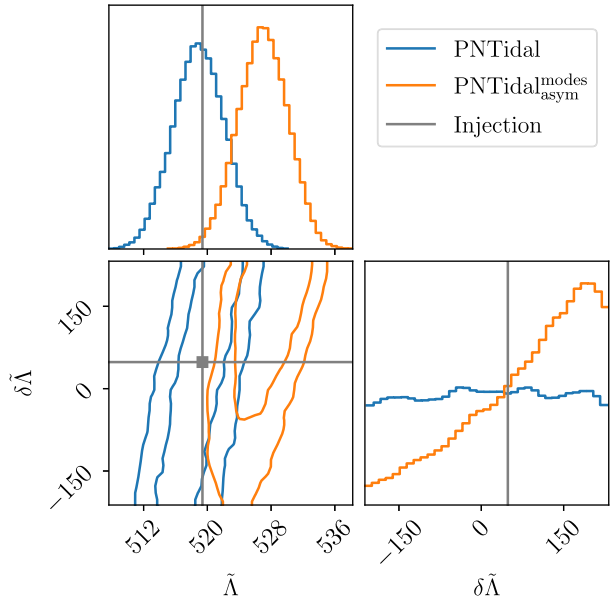

FIG. 9. Gravitomagnetic effects for spin orientations $\psi = \pi/3$ and magnitudes $\chi = 0.005$ at SNR 1800. The blue curve corresponds to using the same waveform for injection and recovery. Comparing this with the orange curve indicates the changes due to gravitomagnetic tides from both the $m = 2$ mode resonances and the adiabatic effects, which lead to a shift in the distribution of $\tilde{\Lambda}$ and a more peaked shape of the $\delta\tilde{\Lambda}$ posterior.

following a similar line of analysis as for the aligned-spin case. We note that the spins are rather small, so we assume that the spin orientation is approximately constant over the inspiral [34].

First, we consider the impact of including all gravitomagnetic effects. From Fig. 9 we see that, even for small spins of $\chi = 0.005$, the gravitomagnetic effects lead to larger shifts in the posterior probability distribution for $\tilde{\Lambda}$ and in the opposite direction compared to the aligned-spin case in Fig. 6. An approximate reasoning for this behavior is that the $m = 2$ resonances occur later in the inspiral than the $m = 1$ resonances, as we will discuss in more depth in Sec. VI. Figure 9 also shows a peak in the distribution for $\delta\Lambda$ when including gravitomagnetic tides (orange curves), however, because the injection neglected gravitomagnetic effects, it is not centered on the injected value.

For higher spins of $\chi = 0.01$, the above trends are more pronounced, as seen in Fig. 10. We observe that the two-dimensional confidence intervals have no overlaps at all in this case, and that the distribution in $\delta\Lambda$ becomes more distinctly peaked.

To gain deeper insights into the reasons for these results, we next characterize the impact of the resonant and adiabatic contributions to gravitomagnetic effects separately. The results of injecting with the full $\mathrm{PNTidal}^{\mathrm{asym}}_{\mathrm{modes}}$ and recovering with different models for cases with smaller and larger spins are shown in the upper and lower panels of

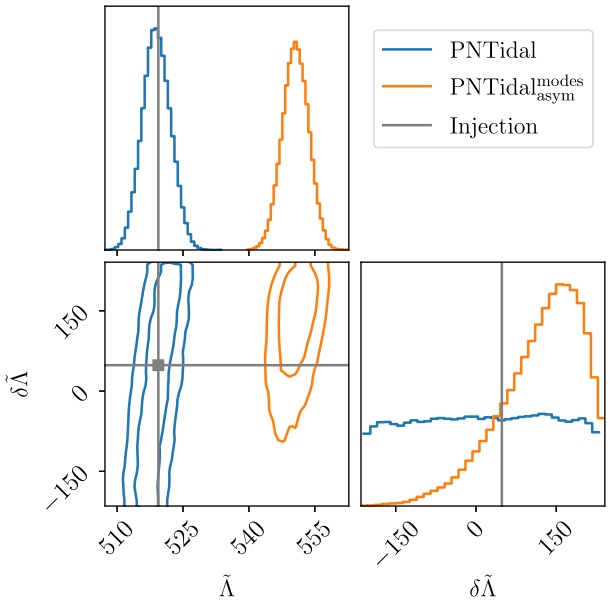

FIG. 10. Gravitomagnetic effects for spin orientations $\psi = \pi/3$ and magnitudes $\chi_{1,2} = 0.01$ at SNR 1800. The blue curve corresponds to using the same waveform for injection and recovery. Comparing this with the orange curve indicates the changes due to gravitomagnetic tides from both the $m = 2$ mode resonances and the adiabatic effects, which lead to a substantial shift in the distribution of $\tilde{\Lambda}$ and clear peak in the $\delta\tilde{\Lambda}$ posterior.

Fig. 11 respectively. We see that the contributions of the $m = 2$ mode resonances (blue curves) are more significant for reducing biases than the adiabatic effects (orange curves) for both the smaller and larger spin magnitudes in this case, though both effects are important to accurately recover the parameters.

D. Measurement accuracy for different spins

Having characterized the importance of the various contributions and gravitomagnetic tides overall, we next compare the net effects on the measurement accuracy for different spin magnitudes. In this study, the injected and recovered waveform is the full PNTidal$^{\text{modes}}_{\text{asym}}$ model with increasing spin $\chi = \{0, 0.005, 0.01\}$. The results for aligned spins are shown in Fig. 12, where the blue, orange, and green curves correspond to spins of 0, 0.005, and 0.01 respectively. We see that changing the spins has very little impact on the posterior distributions for $\tilde{\Lambda}$ in this case. By contrast, a decreasing spin results in a broader distribution in $\delta\tilde{\Lambda}$. As our analysis keeps the spins fixed, the impact of spins is through their coupling with adiabatic tidal parameters through (3.7), the resonance phase shift $\sim\Omega^{2/3}$, and the mode resonance frequency, as we will further discuss in Sec. VI. From the above results, we also infer that the double peak in the distribution of $\delta\tilde{\Lambda}$ for $\chi = 0.005$ arises from the combination of adiabatic and resonant effects, which act in opposite directions, while for $\chi = 0.01$ it is

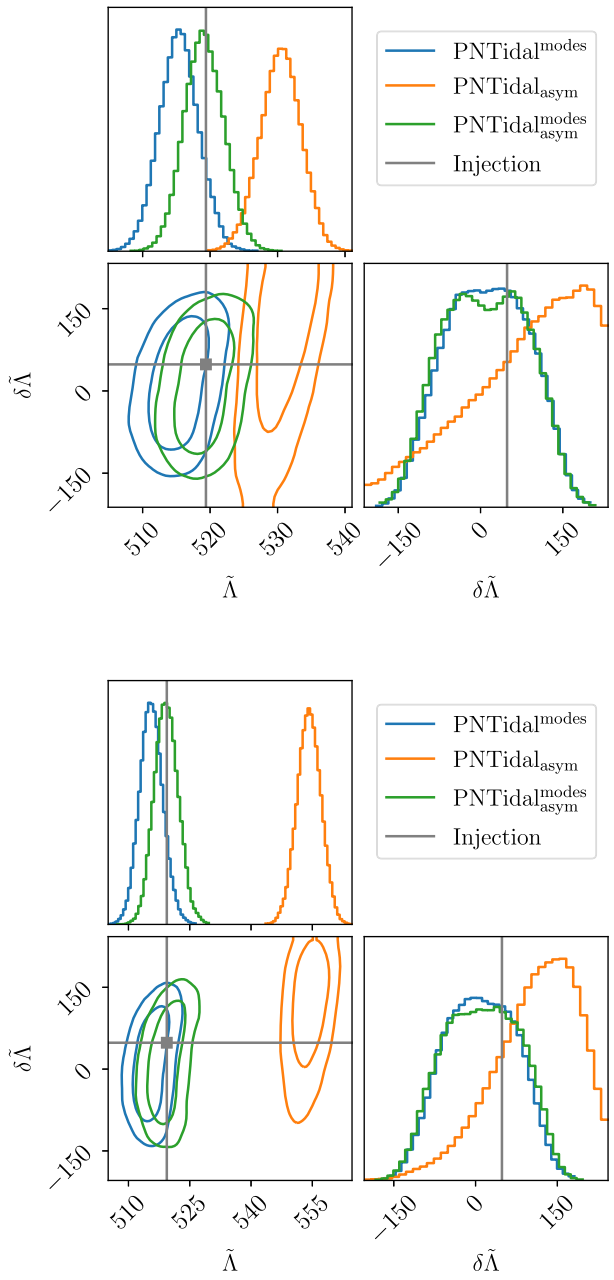

FIG. 11. Effects of various gravitomagnetic contributions on the parameter recovery for misaligned spins. The results are for the systems with SNR 1800 and spin orientations of $\psi = \pi/3$ with $\chi = 0.005$ (upper) and $\chi = 0.01$ (lower). Green curves correspond to recovering with the same full model as the injection, blue curves include only the mode resonances, while orange curves indicate the adiabatic effects. We see that in both cases the mode resonances play a larger role for reducing biases than the adiabatic effects.

largely due to the presence of two resonances spaced widely enough to be noticeable in the data analysis (see also Fig. 8).

A different perspective on the behavior can be gained by considering where in frequency the information about tidal

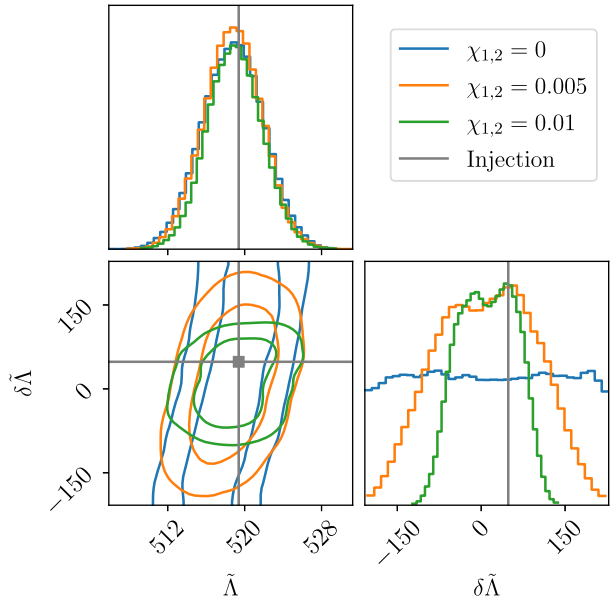

FIG. 12. Effect of the spin magnitude on inferred tidal parameters for aligned spins and SNR of 1800. The injection and recovery both use the same model PNTidal$^{\text{modes}}_{\text{asym}}$ with corresponding spin magnitudes, as indicated in the legend. Increasing the spin magnitude has very little impact on the width of the posterior in $\tilde{\Lambda}$ but significantly affects that of $\delta\tilde{\Lambda}$, where a higher spin leads to tighter bounds.

parameters accumulates. This is not immediately visible from the phasing (3.1a) due to the implicit and nontrivial dependencies of the gravitomagnetic parameters on $\tilde{\Lambda}$ and $\delta\tilde{\Lambda}$ upon using the quasiuniversal relations. Figure 13 shows the normalized integrands entering the Fisher matrix error computations. The resonance frequencies for both neutron stars of aligned spins $\chi = 0.005$ are 12 and 13 Hz. As the frequency becomes equal to the first resonance frequency of 12 Hz, we start to see the effect of mode resonance in both figures for $\tilde{\Lambda}, \delta\tilde{\Lambda}$ and at the second resonance frequency, there is again a sharp change in the normalized integrands. But as it hits zero crossing it rises again which is an artifact of taking the absolute value of integrands. We also see that around 200 Hz there are spikes that are coming from the power spectral density having spikes (Fig. 2). For $\tilde{\Lambda}$, the abrupt changes due to the resonances are too small to be visible on the scale of this plot, which is in contrast to the information on $\delta\tilde{\Lambda}$, where the resonance features are clearly visible.

The corresponding results with varying spin magnitudes for the case with misaligned spins of $\psi = \pi/3$ are shown in Fig. 14. We find similar trends as for the aligned-spin case. However, a notable difference is that, while the presence of spin has the expected impacts on the distributions, the consequences of any change in its magnitude are very small. This is in contrast with the trends in Fig. 12 for the $m = 1$ modes. An explanation of this behavior could potentially come from considering the location of the resonances studied here with respect to the noise curve shown in Fig. 2, where changing the spin has a more drastic impact on the relative location of the $m = 1$ resonances (diamonds) in the detector sensitivity: For $m = 1$ and $\chi = 0.005$ the resonance lies in the frequency regime below ∼20 Hz where the detector sensitivity deteriorates considerably, and for $\chi = 0.01$ it is in the bucket of the

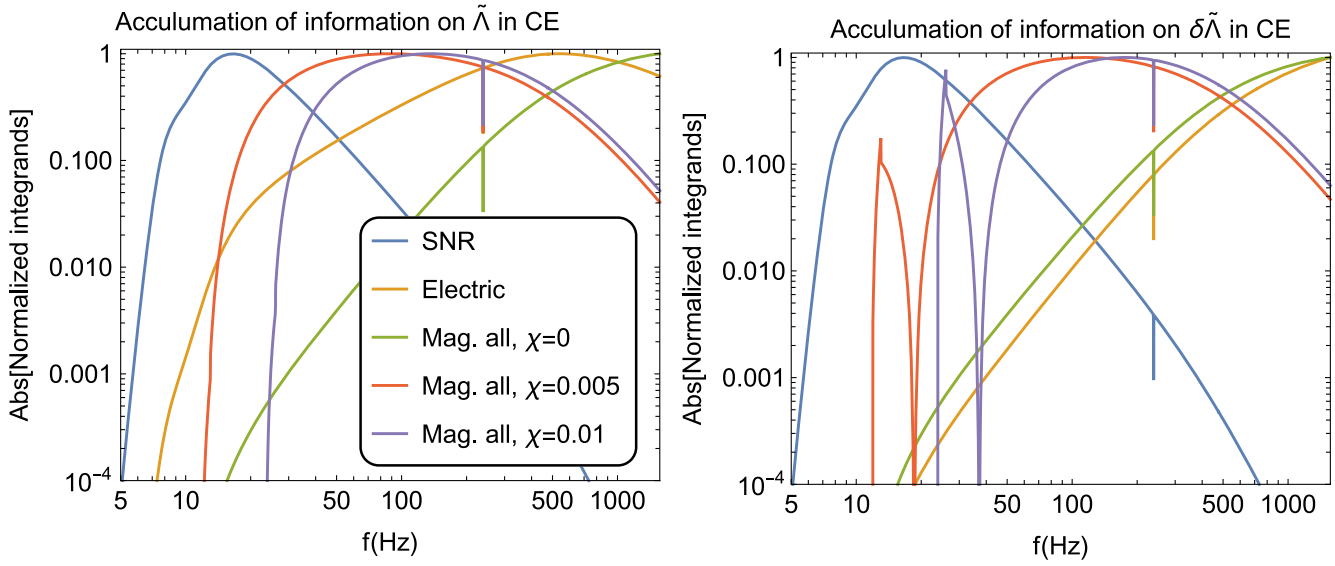

FIG. 13. Accumulation of information encoded in integrands Abs$(\frac{\partial\tilde{h}^{\star}}{\partial\theta_i}\frac{\partial\tilde{h}}{\partial\theta_i} * \frac{1}{S_n(f)})$ (normalized to its maximum value) for $\theta_i = \tilde{\Lambda}$ (left) and $\theta_i = \delta\tilde{\Lambda}$ (right) as a function of frequency for the injected value of aligned spins $\{0.0, 0.005, 0.01\}$, $\tilde{\Lambda} = 519.38$, and $\delta\tilde{\Lambda} = 48.37$. SNR denotes the integrands Abs$(\frac{\tilde{h}^{\star}\tilde{h}}{S_n(f)})$, Electric denotes only adiabatic gravitoelectric tidal contribution in (3.1a), and Mag. all denotes adiabatic and resonant gravitomagnetic tidal contribution in (3.1a).

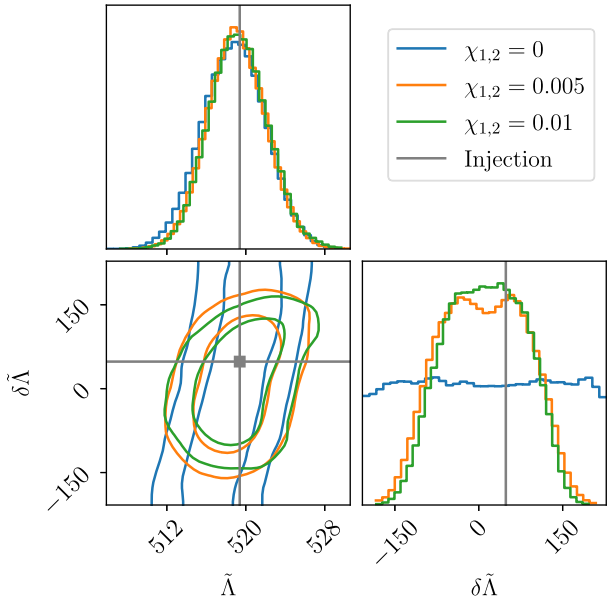

FIG. 14. Effect of the spin magnitude on inferred tidal parameters for inclined spins at 60° and SNR of 1800. The injection and recovery both use the full model PNTidal$^{\text{modes}}_{\text{asym}}$ with varying spin magnitudes as indicated in the legend. Increasing the spin magnitude from a finite value to a higher one has very little impact on the width of the posteriors in this case.

sensitive band, while for $m = 2$ the resonances are in the bucket for both spin values.

1. Extrapolating to lower SNR of 400

Thus far, we have assumed a SNR of 1800 in the CE detector, which is plausible for an event similar to GW170817. However, many more events will be observed at a lower SNR. To estimate the changes in our conclusions for such more numerous events, we perform the same Bayesian analysis as above but for a SNR of 400 instead of 1800. From Fig. 15 we see that for lower SNR the qualitative trends of the effects of increasing the spins remain: there is little impact on the posterior distribution for $\tilde{\Lambda}$, while that for $\delta\tilde{\Lambda}$ becomes tighter. Comparing the left and right panels of Fig. 15, which correspond respectively to the spin orientations where only the $m = 1$ and $m = 2$ modes are present, we also notice that, for the higher spins considered here, the $m = 1$ modes have a larger effect on

TABLE I. Recovered mean and 90% credible intervals of $\tilde{\Lambda}(\delta\tilde{\Lambda})$ for SNR 1800 and 400. The injected values are $\tilde{\Lambda} = 519$ and $\delta\tilde{\Lambda} = 48$. The spin magnitude χ on each NS increases from top to bottom, and we recall that in the aligned-spin case $\psi = 0$ only the $m = 1$ modes pass through resonance, for $\psi = \pi/3$ it is only the $m = 2$ modes, and in the nonspinning case the resonances are absent.

χ	$\psi = 0$	$\psi = \pi/3$
	SNR 1800	SNR 1800
0.0	$518.8^{+5.0}_{-5.3}$ $(10.5^{+193.2}_{-194.2})$	$518.8^{+5.0}_{-5.3}$ $(10.5^{+193.2}_{-194.2})$
0.005	$518.8^{+4.7}_{-4.9}$ $(12.1^{+135.5}_{-143.5})$	$519.1^{+4.8}_{-4.6}$ $(9.2^{+118.5}_{-118.4})$
0.01	$519.0^{+4.7}_{-4.5}$ $(12.1^{+75.6}_{-79.4})$	$519.2^{+4.9}_{-4.6}$ $(12.5^{+106.8}_{-109.7})$
	SNR 400	SNR 400
0.0	$518.9^{+20.6}_{-20.3}$ $(14.6^{+190.1}_{-198.8})$	$518.9^{+20.6}_{-20.3}$ $(14.6^{+190.1}_{-198.8})$
0.005	$519.1^{+20.5}_{-20.5}$ $(10.9^{+191.9}_{-191.6})$	$520.1^{+20.1}_{-20.5}$ $(12.2^{+187.0}_{-191.8})$
0.01	$520.4^{+20.1}_{-20.0}$ $(12.0^{+158.5}_{-162.0})$	$521.1^{+20.0}_{-19.4}$ $(8.4^{+188.3}_{-189.1})$

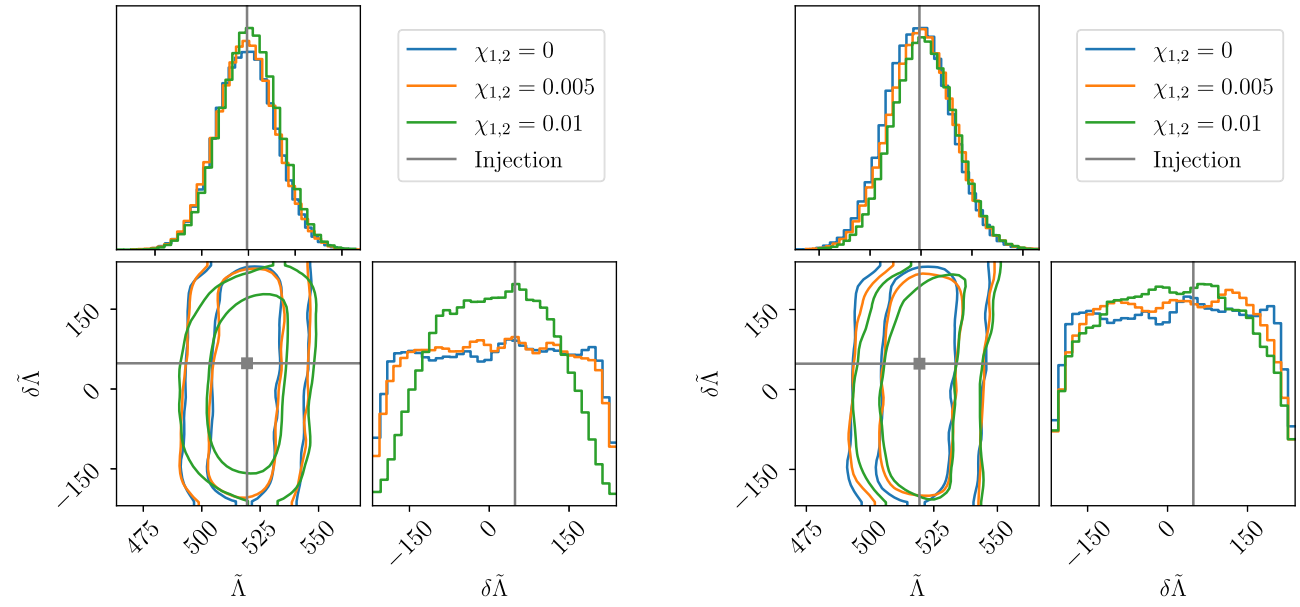

FIG. 15. Bayesian parameter estimation results for systems with SNR 400 for different spins. The injection and recovery both use the model PNTidal$^{\text{modes}}_{\text{asym}}$ with the corresponding spin magnitude indicated in the legend. Left: aligned spins. Right: spin inclinations of 60°. Same as Figs. 12 and 14 except for lower SNR.

the measurability of $\delta\tilde{\Lambda}$ than the $m = 2$ modes. Comparing the results of Fig. 15 with the cases with higher SNR in Figs. 12 and 14 also quantifies the expected trends of a higher SNR resulting in tighter posterior distributions in the parameters. Table I lists the specific values obtained for the mean and 90% credible intervals of the inferred $\tilde{\Lambda}$ and $\delta\tilde{\Lambda}$ distributions. From these results we see that for $\tilde{\Lambda}$, the change in the 90% interval for SNR 400 compared to 1800 is largely consistent with an approximate scaling of the errors as $(\mathrm{SNR})^{-1}$, i.e., the width increases by roughly a factor of ∼4.5. By contrast, the broadening of the 90% interval in $\delta\tilde{\Lambda}$ with lower SNR is significantly less than expected from such a scaling, which is a promising indication for measurements, however, corroborating this for more realistic data analysis implications will require further work.

VI. DISCUSSION

In this section, we discuss interesting aspects of the above findings and their interpretation. The high-level outcome of the case studies in Sec. V is that they corroborate previously disconnected findings [34,60] that gravitomagnetic tidal signatures in the GWs from both adiabatic and resonance-induced effects can have important impacts on the GW phasing for measurements with third-generation detectors. In addition, our analysis provided insights into the quantitative dependencies of these results on different features associated with the resonance-induced and adiabatic contributions and showed that their relative importance strongly depends on the system parameters. We discuss these findings below.

A. Features and parameter dependencies of gravitomagnetic effects in GWs

1. Asymptotic adiabatic effects

The leading-order contribution in the phase is parametrized by the quantity $\tilde{\Sigma}$ in (3.1b), which increases slowly with $\tilde{\Lambda}$ and is positive both before and after a resonance. However, its magnitude significantly drops to much lower values across a resonance. In the GW phase, $\tilde{\Sigma}$ first enters together with $\delta\tilde{\Lambda}$ at the same scaling with frequency and both with the opposite sign as the $\tilde{\Lambda}$ contribution, cf. (3.1b). These effects thus lead to a reduction of the net size of tidal GW signatures. Spin effects coupled with the adiabatic gravitomagnetic effects enter at a higher order in frequency through the parameter $\hat{\Sigma}$, thus contributing new information that breaks the degeneracy with $\delta\tilde{\Lambda}$. For the specific cases considered here, $\hat{\Sigma}$ is positive. The spin orientation impacts the size of the preresonance values of the adiabatic parameters $\tilde{\Sigma}$ and $\hat{\Sigma}$, which can be larger for misaligned spins than for aligned spins.

2. Resonance-induced effects

The resonance effects in the GW phase introduce a behavior that is very different from other contributions to the phasing because of its abruptness. Once present, the scaling with frequency is the same as for the gauge parameters t_c, ϕ_c. The size of the resonance-induced phase shifts depend on the spin magnitude and orientation, as well as the static and irrotational gravitomagnetic Love numbers characterizing how strongly the modes couple to the tidal field. The resonance jumps induce a negative GW phase correction, accelerating the inspiral and increasing the difference to a nontidal signal. This is the opposite behavior as the leading-order adiabatic effects from gravitomagnetic tides discussed above. The resonance effects increase with larger $\tilde{\Lambda}$ and decrease for larger $\delta\tilde{\Lambda}$. Furthermore, larger spins lead to larger resonance jumps, as also seen from the spin dependence of (3.10), where $\Delta\Phi_{2m} \sim \chi^{2/3}$, and where we also note that the dependence on the spin orientation is such that $\Delta\Phi_{2m}$ is largest for aligned spins. In addition, the resonance frequencies are approximately proportional to the spin frequency as well as the mode number m. Larger spins and m shift the resonances to higher frequencies, which can have several consequences depending on the resonance location. For example, for the case studies considered here, a shift of the resonances to higher frequencies leads to an enhanced accumulation of information from the preresonance adiabatic effects, the resonance jumps being within regimes of greater detector sensitivity, and a reduction in the number of cycles over which information from the resonances accumulates. As expected, when resonances occur within the most sensitive band of the detector, which in Sec. V were the cases with $\chi = 0.01$ and the scenario with $\chi = 0.005$ with spins misaligned by 60°, the relative importance of the resonance effects is larger.

B. Case studies of aligned-spin systems

For systems with aligned spins, we found different trends depending on the spin magnitudes. In the nonspinning case, only the adiabatic postresonance effects contribute to the GW phase. As explained above, the leading-order adiabatic gravitomagnetic parameter $\tilde{\Sigma}$ contributes to the phasing (3.1b) in the same way as $\delta\tilde{\Lambda}$, while the contribution from $\hat{\Sigma}$ vanishes for zero spins. Consequently, gravitomagnetic effects have a rather small impact on the measurability of $\delta\tilde{\Lambda}$, as also seen in Fig. 5. Furthermore, the $\tilde{\Sigma}$-dependent contribution effectively reduces the size of the tidal effects in the phasing, which in the Bayesian analysis leads to the shift of the recovered $\tilde{\Lambda}$ to lower values, as also seen in Fig. 5.

For finite but low spins of $\chi = 0.005$, the gravitomagnetic mode resonances occur at the lower end of CE's sensitive band, cf. Fig. 2, where the sensitivity is deteriorating. As seen in the upper panel of Fig. 8, we find that in

this case the dominant contribution for recovering the correct mean for $\tilde{\Lambda}$ is the postresonance asymptotic values. Consequently, the results for $\tilde{\Lambda}$ shown in Fig. 6 are similar to the nonspinning case in Fig. 5. When compared to the full baseline model with all gravitomagnetic effects, the mode resonances tend to lead to lower $\tilde{\Lambda}$ mean values, while adiabatic effects shift the distribution more toward higher ones in this case. A new feature with spins is that the $\delta\tilde{\Lambda}$ distribution becomes less flat, implying that this parameter becomes measurable, albeit with much larger statistical errors than $\tilde{\Lambda}$. As seen from Fig. 8, a nonflat distribution arises from both adiabatic effects and resonance jumps, however, the contribution from the latter is larger in this case.

For the higher spin system with $\chi = 0.01$, where the resonances occur at higher frequencies, the posterior in $\tilde{\Lambda}$ with all gravitomagnetic effects is shifted in the opposite direction relative to the gravitoelectric baseline than the case with lower spins $\chi = 0.005$, as seen by comparing Figs. 6 and 7. This is due to the resonance effects becoming the dominant contribution to the results for $\tilde{\Lambda}$, as seen in the lower panel of Fig. 8. Interestingly, the measurement of $\delta\tilde{\Lambda}$ in this higher spin case is impacted nearly equally by both adiabatic and resonance effects, in which both give similarly tight posteriors. We attribute the enhanced contribution from adiabatic effects for higher spins primarily to the larger contribution from $\hat{\Sigma}$, which breaks the degeneracies, with a potential further enhancement due to the resonance occurring at higher frequency, which increases the importance of the larger preresonance contribution to $\tilde{\Sigma}(\tilde{\Lambda}, \delta\tilde{\Lambda})$, making the effects larger overall.

C. Spins inclined at 60°

The system with misaligned spins of $\chi = 0.005$ we considered has the same resonance frequencies as the case study of aligned spins with $\chi = 0.01$. However, the other parameters of these systems differ, which enables us to study their dependencies for a fixed resonance location. Specifically, the value of the phase jumps $\Delta\Phi_{2m}$ from (3.10) are about 4 times larger for the high-spin $m = 1$ case than for $m = 2$ with low spin. Conversely, in the same comparison, $|\hat{\Sigma}|$ is smaller by a factor of about 2 for the preresonance regime. The pre- and postresonance values of $\tilde{\Sigma}$ are the same in the two cases. The outcomes of our analysis for the $m = 2$ case with low spins are indeed qualitatively similar to that with the same resonance location but aligned spins. Notably, we find that the gravitomagnetic effects lead to a significant shift in $\tilde{\Lambda}$ compared to the gravitoelectric baseline and to a nonflat distribution of $\delta\tilde{\Lambda}$. Overall, the effects are larger for aligned high spins than for the misaligned low-spin case, as can be seen by comparing, for example, Figs. 7 and 9.

For the case of misaligned spins with $\chi = 0.01$, the results are similar to those with the lower spin magnitudes, as seen in Fig. 14. This is in contrast to the aligned-spin case, where an increasing spin magnitude changes the importance of different gravitomagnetic contributions and noticeably improves the measurability as seen in Fig. 12, for reasons explained above.

VII. CONCLUSION

In this work, we developed an approximate but efficient adaptation of known results to incorporate more realistic descriptions of resonant and adiabatic gravitomagnetic tidal effects in the Fourier-domain GW phasing. Our results assume slowly rotating neutron stars and focus on the quadrupolar effects. We discussed the subtleties with gravitomagnetic adiabatic effects, where calculations based on relativistic perturbation theory identified two different characteristic tidal deformability parameters. We derived the combinations of these parameters that appear together with a dependence on the spin orientation and the normalized mode frequencies in the GW signals. Interestingly, these combinations are different before and after a mode resonance. We also showed how to adapt an existing model for the resonance-induced GW phase shift to incorporate the fully relativistic properties of NSs. In general, each NS passes through two quadrupolar gravitomagnetic resonances corresponding to the $m = 1$ and $m = 2$ modes, which for spins of $\chi \gtrsim 0.005$ lie within the sensitive band of third-generation GW detectors.

We used the above model to perform a data analysis study of the impact of gravitomagnetic effects on the measurements of tidal parameters with third-generation GW detectors, which relied on several simplifying assumptions. In particular, we used quasiuniversal relations to reduce all matter parameters to the two tidal deformabilities, considered neutron stars with slightly unequal masses but equal spins and orientations such that only one set of modes is resonantly excited during the inspiral, and mainly adopted a Bayesian approach restricted to a four-dimensional subspace of parameters for GW170817-like events. These case studies enabled us to gain several quantitative insights and demonstrated that gravitomagnetic tides can be important to avoid biases in the inferred $\tilde{\Lambda}$ and lead to a peaked distribution in $\delta\tilde{\Lambda}$, which is flat and thus uninformative when neglecting gravitomagnetic effects.

To gain further insights into the underlying reasons for these results, we analyzed the different contributions to the gravitomagnetic tides, adiabatic versus resonance induced, and compared the impacts of the $m = 1$ and $m = 2$ modes. In the configurations considered here, the $m = 1$ ($m = 2$) modes were relevant for aligned (60° inclined) spins. We found that for the $m = 1$ modes, increasing the spin leads to increasingly better measurements of the tidal parameters. Furthermore, for aligned spins of magnitude $\chi = 0.005$, the adiabatic effects are most important to avoid biases in the

parameter $\tilde{\Lambda}$, while for larger spins of $\chi = 0.01$ it is the mode resonances. In all cases, the mode resonances have a significant impact on the measurability of $\delta\tilde{\Lambda}$. On the other hand, for spin orientations where only the $m = 2$ modes are resonant, we found no significant changes in the results with increasing spins.

We also considered a case with a lower SNR of 400, as is expected for a larger number of events, and found that similar qualitative trends persist. Interestingly, we noticed that, while the broadening of the inferred posterior probability distribution seems to scale inversely with the SNR, the broadening of the posterior in $\delta\tilde{\Lambda}$ is much less than this scaling. This is a promising indication for future measurements but will need to be confirmed with more realistic data analysis studies.

In conclusion, our work represents an exploratory study based on more realistic modeling of gravitomagnetic tides than in previous work. We made several simplifying assumptions and approximations and neglected a number of additional matter effects that impact the GWs. Our results about the importance of the gravitomagnetic effects for measurements motivate more detailed data analysis studies as well as further advances in the modeling, which we leave to future work.

ACKNOWLEDGMENTS

This work was supported by the Netherlands Organization for Scientific Research (NWO). T. H. acknowledges support from the NWO sector plan.

[1] B. P. Abbott *et al.* (LIGO Scientific and Virgo Collaborations), GW170817: Observation of gravitational waves from a binary neutron star inspiral, Phys. Rev. Lett. **119**, 161101 (2017).
[2] Ani Aprahamian *et al.*, Reaching for the horizon: The 2015 long range plan for nuclear science (2015), https://inspirehep.net/literature/1398831.
[3] Angela Bracco, NuPECC long range plan on perspectives in nuclear physics, Europhys. News **48/4**, 21 (2017).
[4] J. Aasi *et al.* (LIGO Scientific Collaboration), Advanced LIGO, Classical Quantum Gravity **32**, 074001 (2015).
[5] F. Acernese *et al.* (Virgo Collaboration), Advanced Virgo: A second-generation interferometric gravitational wave detector, Classical Quantum Gravity **32**, 024001 (2015).
[6] Yoichi Aso, Yuta Michimura, Kentaro Somiya, Masaki Ando, Osamu Miyakawa, Takanori Sekiguchi, Daisuke Tatsumi, and Hiroaki Yamamoto (KAGRA Collaboration), Interferometer design of the KAGRA gravitational wave detector, Phys. Rev. D **88**, 043007 (2013).
[7] B. P. Abbott *et al.* (KAGRA, LIGO Scientific, and Virgo Collaborations), Prospects for observing and localizing gravitational-wave transients with Advanced LIGO, Advanced Virgo and KAGRA, Living Rev. Relativity **21**, 3 (2018).
[8] M. Punturo *et al.*, The third generation of gravitational wave observatories and their science reach, Classical Quantum Gravity **27**, 084007 (2010).
[9] David Reitze *et al.*, Cosmic Explorer: The U.S. contribution to gravitational-wave astronomy beyond LIGO, Bull. Am. Astron. Soc. **51**, 035 (2019), https://ui.adsabs.harvard.edu/abs/2019BAAS...51g..35R/abstract.
[10] Michele Maggiore *et al.*, Science case for the Einstein Telescope, J. Cosmol. Astropart. Phys. 03 (2020) 050.
[11] B. S. Sathyaprakash *et al.*, Extreme gravity and fundamental physics, arXiv:1903.09221.
[12] Vicky Kalogera *et al.*, The next generation global gravitational wave observatory: The science book, arXiv:2111.06990.
[13] Benjamin P. Abbott *et al.* (LIGO Scientific and Virgo Collaborations), A guide to LIGO–Virgo detector noise and extraction of transient gravitational-wave signals, Classical Quantum Gravity **37**, 055002 (2020).
[14] B. P. Abbott *et al.* (LIGO Scientific and Virgo Collaborations), GWTC-1: A gravitational-wave transient catalog of compact binary mergers observed by LIGO and Virgo during the first and second observing runs, Phys. Rev. X **9**, 031040 (2019).
[15] Michael Pürrer and Carl-Johan Haster, Gravitational waveform accuracy requirements for future ground-based detectors, Phys. Rev. Res. **2**, 023151 (2020).
[16] Yiwen Huang, Carl-Johan Haster, Salvatore Vitale, Vijay Varma, Francois Foucart, and Sylvia Biscoveanu, Statistical and systematic uncertainties in extracting the source properties of neutron star–black hole binaries with gravitational waves, Phys. Rev. D **103**, 083001 (2021).
[17] Qian Hu and John Veitch, Assessing the model waveform accuracy of gravitational waves, Phys. Rev. D **106**, 044042 (2022).
[18] Jocelyn S. Read, Waveform uncertainty quantification and interpretation for gravitational-wave astronomy, Classical Quantum Gravity **40**, 135002 (2023).
[19] Alberto Mangiagli, Antoine Klein, Alberto Sesana, Enrico Barausse, and Monica Colpi, Post-Newtonian phase accuracy requirements for stellar black hole binaries with LISA, Phys. Rev. D **99**, 064056 (2019).
[20] Caroline B. Owen, Carl-Johan Haster, Scott Perkins, Neil J. Cornish, and Nicolás Yunes, Waveform accuracy and systematic uncertainties in current gravitational wave observations, Phys. Rev. D **108**, 044018 (2023).
[21] Eanna E. Flanagan and Tanja Hinderer, Constraining neutron star tidal Love numbers with gravitational wave detectors, Phys. Rev. D **77**, 021502 (2008).
[22] Jan Steinhoff, Tanja Hinderer, Alessandra Buonanno, and Andrea Taracchini, Dynamical tides in general relativity:

Effective action and effective-one-body Hamiltonian, Phys. Rev. D **94**, 104028 (2016).
[23] Geraint Pratten, Patricia Schmidt, and Natalie Williams, Impact of dynamical tides on the reconstruction of the neutron star equation of state, Phys. Rev. Lett. **129**, 081102 (2022).
[24] Kostas D. Kokkotas and Bernd G. Schmidt, Quasinormal modes of stars and black holes, Living Rev. Relativity **2**, 2 (1999).
[25] Nils Andersson and Kostas D. Kokkotas, The R mode instability in rotating neutron stars, Int. J. Mod. Phys. D **10**, 381 (2001).
[26] Ashikuzzaman Idrisy, Benjamin J. Owen, and David I. Jones, *R*-mode frequencies of slowly rotating relativistic neutron stars with realistic equations of state, Phys. Rev. D **91**, 024001 (2015).
[27] Umin Lee and Shijun Yoshida, R-modes of neutron stars with the superfluid core, Astrophys. J. **586**, 403 (2003).
[28] Kostas D. Kokkotas and Kai Schwenzer, R-mode astronomy, Eur. Phys. J. A **52**, 38 (2016).
[29] J. Provost, G. Berthomieu, and A. Rocca, Low frequency oscillations of a slowly rotating star–quasi toroidal modes, Astron. Astrophys. **94**, 126 (1981), https://adsabs.harvard.edu/full/1981A%26A....94..126P.
[30] Wynn C. G. Ho and Dong Lai, Resonant tidal excitations of rotating neutron stars in coalescing binaries, Mon. Not. R. Astron. Soc. **308**, 153 (1999).
[31] A. Katrin Schenk, Phil Arras, Eanna E. Flanagan, Saul A. Teukolsky, and Ira Wasserman, Nonlinear mode coupling in rotating stars and the *r*-mode instability in neutron stars, Phys. Rev. D **65**, 024001 (2002).
[32] Keith H. Lockitch and John L. Friedman, Where are the r modes of isentropic stars?, Astrophys. J. **521**, 764 (1999).
[33] Eanna E. Flanagan and Etienne Racine, Gravitomagnetic resonant excitation of Rossby modes in coalescing neutron star binaries, Phys. Rev. D **75**, 044001 (2007).
[34] Sizheng Ma, Hang Yu, and Yanbei Chen, Detecting resonant tidal excitations of Rossby modes in coalescing neutron-star binaries with third-generation gravitational-wave detectors, Phys. Rev. D **103**, 063020 (2021).
[35] Eric Poisson, Gravitomagnetic tidal resonance in neutron-star binary inspirals, Phys. Rev. D **101**, 104028 (2020).
[36] Eric Poisson, Gravitomagnetic Love tensor of a slowly rotating body: Post-Newtonian theory, Phys. Rev. D **102**, 064059 (2020).
[37] Hang Yu and Nevin N. Weinberg, Dynamical tides in coalescing superfluid neutron star binaries with hyperon cores and their detectability with third generation gravitational-wave detectors, Mon. Not. R. Astron. Soc. **470**, 350 (2017).
[38] Miquel Miravet-Tenés, Florencia L. Castillo, Roberto De Pietri, Pablo Cerdá-Durán, and José A. Font, Prospects for the inference of inertial modes from hypermassive neutron stars with future gravitational-wave detectors, Phys. Rev. D **107**, 103053 (2023).
[39] Xisco Jiménez Forteza, Tiziano Abdelsalhin, Paolo Pani, and Leonardo Gualtieri, Impact of high-order tidal terms on binary neutron-star waveforms, Phys. Rev. D **98**, 124014 (2018).
[40] Sarp Akcay, Sebastiano Bernuzzi, Francesco Messina, Alessandro Nagar, Néstor Ortiz, and Piero Rettegno, Effective-one-body multipolar waveform for tidally interacting binary neutron stars up to merger, Phys. Rev. D **99**, 044051 (2019).
[41] Thibault Damour and Alessandro Nagar, Relativistic tidal properties of neutron stars, Phys. Rev. D **80**, 084035 (2009).
[42] Taylor Binnington and Eric Poisson, Relativistic theory of tidal Love numbers, Phys. Rev. D **80**, 084018 (2009).
[43] Philippe Landry and Eric Poisson, Gravitomagnetic response of an irrotational body to an applied tidal field, Phys. Rev. D **91**, 104026 (2015).
[44] Philippe Landry and Eric Poisson, Dynamical response to a stationary tidal field, Phys. Rev. D **92**, 124041 (2015).
[45] Eric Poisson and Jean Doucot, Gravitomagnetic tidal currents in rotating neutron stars, Phys. Rev. D **95**, 044023 (2017).
[46] Paolo Pani, Leonardo Gualtieri, Tiziano Abdelsalhin, and Xisco Jiménez-Forteza, Magnetic tidal Love numbers clarified, Phys. Rev. D **98**, 124023 (2018).
[47] Pawan Kumar Gupta, Jan Steinhoff, and Tanja Hinderer, Relativistic effective action of dynamical gravitomagnetic tides for slowly rotating neutron stars, Phys. Rev. Res. **3**, 013147 (2021).
[48] Kent Yagi, Multipole Love relations, Phys. Rev. D **89**, 043011 (2014); **96**, 129904(E) (2017); **97**, 129901(E) (2018).
[49] Lawrence E. Kidder, Coalescing binary systems of compact objects to $(\text{post})^{5/2}$-Newtonian order. V. Spin effects, Phys. Rev. D **52**, 821 (1995).
[50] Kip S. Thorne, Multipole expansions of gravitational radiation, Rev. Mod. Phys. **52**, 299 (1980).
[51] Mark Hannam, Patricia Schmidt, Alejandro Bohé, Leïla Haegel, Sascha Husa, Frank Ohme, Geraint Pratten, and Michael Pürrer, Simple model of complete precessing black-hole-binary gravitational waveforms, Phys. Rev. Lett. **113**, 151101 (2014).
[52] Sascha Husa, Sebastian Khan, Mark Hannam, Michael Pürrer, Frank Ohme, Xisco Jiménez Forteza, and Alejandro Bohé, Frequency-domain gravitational waves from nonprecessing black-hole binaries. I. New numerical waveforms and anatomy of the signal, Phys. Rev. D **93**, 044006 (2016).
[53] Sebastian Khan, Sascha Husa, Mark Hannam, Frank Ohme, Michael Pürrer, Xisco Jiménez Forteza, and Alejandro Bohé, Frequency-domain gravitational waves from nonprecessing black-hole binaries. II. A phenomenological model for the advanced detector era, Phys. Rev. D **93**, 044007 (2016).
[54] Alessandra Buonanno, Bala Iyer, Evan Ochsner, Yi Pan, and B. S. Sathyaprakash, Comparison of post-Newtonian templates for compact binary inspiral signals in gravitational-wave detectors, Phys. Rev. D **80**, 084043 (2009).
[55] Tanja Hinderer, Tidal Love numbers of neutron stars, Astrophys. J. **677**, 1216 (2008).
[56] Justin Vines, Eanna E. Flanagan, and Tanja Hinderer, Post-1-Newtonian tidal effects in the gravitational waveform from binary inspirals, Phys. Rev. D **83**, 084051 (2011).
[57] Thibault Damour, Alessandro Nagar, and Loic Villain, Measurability of the tidal polarizability of neutron stars

in late-inspiral gravitational-wave signals, Phys. Rev. D **85**, 123007 (2012).

[58] Quentin Henry, Guillaume Faye, and Luc Blanchet, Tidal effects in the gravitational-wave phase evolution of compact binary systems to next-to-next-to-leading post-Newtonian order, Phys. Rev. D **102**, 044033 (2020).

[59] Batoul Banihashemi and Justin Vines, Gravitomagnetic tidal effects in gravitational waves from neutron star binaries, Phys. Rev. D **101**, 064003 (2020).

[60] Xisco Jiménez Forteza, Tiziano Abdelsalhin, Paolo Pani, and Leonardo Gualtieri, Impact of high-order tidal terms on binary neutron-star waveforms, Phys. Rev. D **98**, 124014 (2018).

[61] Pawan Kumar Gupta, Anna Puecher, Peter T. H. Pang, Justin Janquart, Gideon Koekoek, and Chris Broeck Van Den, Determining the equation of state of neutron stars with Einstein Telescope using tidal effects and r-mode excitations from a population of binary inspirals, arXiv:2205.01182.

[62] Daniel Foreman-Mackey, David W. Hogg, Dustin Lang, and Jonathan Goodman, EMCEE: The MCMC hammer, Publ. Astron. Soc. Pac. **125**, 306 (2013).

[63] Benjamin P Abbott *et al.* (LIGO Scientific Collaboration), Exploring the sensitivity of next generation gravitational wave detectors, Classical Quantum Gravity **34**, 044001 (2017).

[64] B. P. Abbott *et al.* (LIGO Scientific and Virgo Collaborations), GW170817: Measurements of neutron star radii and equation of state, Phys. Rev. Lett. **121**, 161101 (2018).

[65] Kent Yagi and Nicolas Yunes, I-Love-Q, Science **341**, 365 (2013).

[66] Tim Dietrich, Sebastiano Bernuzzi, and Wolfgang Tichy, Closed-form tidal approximants for binary neutron star gravitational waveforms constructed from high-resolution numerical relativity simulations, Phys. Rev. D **96**, 121501 (2017).

[67] LIGO Scientific Collaboration, LIGO Algorithm Library—LALSuite, free software (GPL) (2018), https://doi.org/10.7935/GT1W-FZ16.

[68] C. M. Biwer, Collin D. Capano, Soumi De, Miriam Cabero, Duncan A. Brown, Alexander H. Nitz, and V. Raymond, PyCBC Inference: A Python-based parameter estimation toolkit for compact binary coalescence signals, Publ. Astron. Soc. Pac. **131**, 024503 (2019).